JGR Space Physics

RESEARCH ARTICLE
10.1029/2022JA030968

Inner Belt Wisp Precipitation Measured by ELFIN: Regimes of Energetic Electron Scattering by VLF Transmitter Waves

Yangyang Shen[1], Anton V. Artemyev[1], Qianli Ma[2,3], Xiao-Jia Zhang[1,4], Didier Mourenas[5,6], Ethan Tsai[1], Colin Wilkins[1], Jiashu Wu[1], and Vassilis Angelopoulos[1]

[1]Department of Earth, Planetary, and Space Sciences, University of California, Los Angeles, Los Angeles, CA, USA, [2]Department of Atmospheric and Oceanic Sciences, University of California, Los Angeles, Los Angeles, CA, USA, [3]Center for Space Physics, Boston University, Boston, MA, USA, [4]Department of Physics, University of Texas at Dallas, Richardson, TX, USA, [5]CEA, DAM, DIF, Arpajon, France, [6]Laboratoire Matière en Conditions Extrêmes, Paris-Saclay University, CEA, Bruyères-le-Châtel, France

Key Points:

- We report statistical observations of inner belt wisps with full pitch angle distributions measured by Electron Loss and Fields Investigation
- Local bounce-loss-cone wisp precipitation events allow inference of quasilinear diffusion rates and transmitter wave amplitudes
- Inferred transmitter wave amplitudes exceed nonlinear interaction threshold amplitudes near the equator

Supporting Information:

Supporting Information may be found in the online version of this article.

Correspondence to:

Y. Shen,
yshen@epss.ucla.edu

Citation:

Shen, Y., Artemyev, A. V., Ma, Q., Zhang, X.-J., Mourenas, D., Tsai, E., et al. (2022). Inner belt wisp precipitation measured by ELFIN: Regimes of energetic electron scattering by VLF transmitter waves. *Journal of Geophysical Research: Space Physics*, *127*, e2022JA030968. https://doi.org/10.1029/2022JA030968

Received 2 SEP 2022
Accepted 5 NOV 2022

Abstract Man-made very low frequency (VLF) transmitter waves play a critical role in energetic electron scattering and precipitation from the inner radiation belt, a type of which is called wisp precipitation. Wisps exhibit dispersive energy-versus-L spectra due to the evolution of electron cyclotron resonance conditions with near-monochromatic VLF transmitter waves. Here, we report on such observations of inner belt wisp precipitation events with full pitch angle resolution in the energy range of 50 to ~500 keV as measured by Electron Loss and Fields Investigation (ELFIN) at $L < \sim 2$ between March 2021 and April 2022. Statistical observations (82 events) reveal occasional (18 events) wisp precipitation events with local bounce-loss-cone electron flux enhancements, which provide new information compared with flux enhancements measured in previous studies only in the drift loss cone. Based on magnetic field and plasmaspheric density models, quasilinear theory, and detailed pitch angle distributions of wisps from ELFIN, we have estimated the wisp electron bounce-averaged pitch angle diffusion coefficients to be of the order of 10^{-4} to 10^{-2} s^{-1}. These are several orders of magnitude larger than the diffusion rates calculated from models using global statistical averages of VLF transmitter wave power. When using our estimated diffusion coefficients to deduce the associated local transmitter wave amplitudes near the equator, based on quasilinear calculations from a transmitter-induced electron diffusion model, we find these wave amplitudes to be >1 mV/m. Although probable overestimates, such inferred wave amplitudes exceed the theoretical threshold amplitude for nonlinear interactions, strongly suggesting that it is necessary to include nonlinear effects for an accurate evaluation of energetic electron scattering by transmitter waves.

Plain Language Summary Man-made ground-based very low frequency (VLF) transmitter waves can scatter and precipitate energetic radiation belt electrons, which pose a threat to telecommunication and human assets in space. Therefore, understanding the controlling parameters and the efficiency of energetic electron scattering by VLF transmitter waves are of both theoretical and practical importance. Our paper reports statistical analyses of inner belt wisp precipitation events due to scattering by VLF transmitter waves as observed by the Electron Loss and Fields Investigation CubeSats. Occasional strong local wisp precipitation events have been found to occur at preferential longitudes east of the South Atlantic Anomaly in the Northern Hemisphere and were primarily observed in the morning magnetic local time. These local wisp precipitation events have been used to infer energetic electron diffusion rates and VLF transmitter wave amplitudes near the equator based on quasilinear diffusion theory. Such inferred wave amplitudes exceed the theoretical threshold amplitude for nonlinear interactions, strongly suggesting that it is necessary to include nonlinear effects for an accurate evaluation of energetic electron scattering by transmitter waves.

1. Introduction

Anthropogenic ground-based very low frequency (VLF) transmitters radiate essentially monochromatic emissions in the frequency range of 10–30 kHz with high power from ~20 kW to 2 MW (Gu et al., 2021; Helliwell & Katsufrakis, 1974; Imhof et al., 1983; Koons et al., 1981; Ma et al., 2017; Meredith et al., 2019; Sauvaud et al., 2008; Starks et al., 2020; Vampola & Kuck, 1978). These transmitted VLF waves can propagate to long distances within the Earth–ionosphere waveguide before they leak through the inhomogeneous ionosphere and travel as whistler-mode waves in the magnetosphere (Helliwell, 1965; Kulkarni et al., 2008; Lehtinen &

Inan, 2009; Starks et al., 2008). Near the equatorial magnetosphere, VLF transmitter waves can scatter electrons in pitch angle through the first-order cyclotron resonance (see, e.g., Datlowe & Imhof, 1990; Sauvaud et al., 2008; Vampola & Kuck, 1978) and thus have been suggested to play a crucial role in energetic electron losses at $L < 2.5$ from the inner belt (Abel & Thorne, 1998; Agapitov et al., 2014; Albert et al., 2020; Claudepierre et al., 2020; Hua et al., 2020; Ma et al., 2017; Ross et al., 2019).

Direct evidence of transmitter-induced energetic precipitation first came from a controlled VLF modulation experiment by Imhof et al. (1983), in which the VLF transmitter at Cutler, Maine (NAA, 1 MW) was modulated with a repeated ON (3-s)/OFF (2-s) pattern. After the start of ON pulse, correlated enhancements of energetic electron fluxes in the bounce loss cone (BLC) were recorded at $L \sim 2.2$ by the SEEP payload. This transmitter-induced BLC precipitation, however, was suggested to be uncommon and was observed only during high-power transmission intervals. Most other studies have reported only drift-loss-cone (DLC) electron precipitation associated with man-made VLF waves (Datlowe & Imhof, 1990; Gamble et al., 2008; Koons et al., 1981; X. Li et al., 2012; Liu et al., 2022; Sauvaud et al., 2008). DLC electrons are quasi-trapped electrons which are bound to precipitate into the South Atlantic Anomaly (SAA) where the electron drift shells intersect the top of the atmosphere due to the offset of the axis of the geomagnetic field from the center of the Earth (Datlowe & Imhof, 1990). Since electron fluxes are usually higher at higher pitch angles, electron flux enhancements just inside the DLC are easier to detect than at lower pitch angles within the BLC, although quasilinear theory also predicts precipitation within the BLC (Kennel & Petschek, 1966; W. Li, Ni, et al., 2013). In addition, many past satellites have sampled only higher pitch angles outside the BLC. An outstanding type of DLC precipitation attributed to VLF transmitter waves is the so-called wisp, the occurrence of which has been often associated with the most powerful North West Cape (NWC, 1 MW) transmitter at $L \sim 1.4$ (Gamble et al., 2008; Sauvaud et al., 2008).

Wisp precipitation features enhanced electron fluxes with narrow spectral peaks at resonant energies which dispersively decrease with increasing L-shells in the inner belt region ($L \sim 1.5$–2.1; Sauvaud et al., 2008). The narrow spectra and coherent precipitation are consistent with electron first-order cyclotron resonant interactions with nearly monochromatic VLF waves at different L-shells (Selesnick et al., 2013). Most previous wisp observations were obtained from the DEMETER mission, which only provides quasi-trapped electron flux measurements near 90° pitch angles (Sauvaud et al., 2006). Thus, it remains unclear whether and how much BLC electron fluxes are associated with wisps. Because elevated DLC electron fluxes can be contributed by either local scattering or cumulative scattering along their eastward drift paths (Datlowe & Imhof, 1990; Koons et al., 1981; Sauvaud et al., 2008), additional information on the BLC precipitation is critical to our understanding of local wave–particle interaction processes associated with individual VLF transmitter waves. A better understanding of local interactions between transmitter waves and inner belt electrons is important for radiation belt electron remediation. In this paper, we will report observations of BLC wisp precipitation events measured from the Electron Loss and Fields Investigation (ELFIN) twin CubeSats (Angelopoulos et al., 2020).

To fully understand and model the contribution of VLF waves to energetic electron precipitation from the inner belt, one needs to obtain accurate information on VLF transmitter wave intensities (Abel & Thorne, 1998; Hua et al., 2020; Ma et al., 2017; Meredith et al., 2019; Starks et al., 2020), wave normal angles (WNAs; Gu et al., 2021; Ma et al., 2017, 2022; Ross et al., 2019; Z. Zhang et al., 2018), and spatial distributions near the equatorial magnetosphere (Meredith et al., 2019) where wave–particle interactions primarily take place. Much debate has been focused on whether VLF transmitter waves propagate in ducted (with quasi-parallel WNAs <30°) or nonducted mode in previous observational and ray-tracing studies (Agapitov et al., 2014; Clilverd et al., 2008; Gamble et al., 2008; Gu et al., 2021; Inan et al., 2007; Kulkarni et al., 2008; Ma et al., 2017; Z. Zhang et al., 2018). Using wave-induced precipitation models along with ray-tracing simulations (Kulkarni et al., 2008), Inan et al. (2007) have shown evidence of modulated energetic electron precipitation at $L \sim 2$ produced by modulated Hawaii NPM VLF transmissions at $L \sim 1.2$. The energetic electron precipitation was confirmed by the detection of the induced amplitude and phase modulations of NLK and NLM signals at relatively higher L-shells ($L > 2$). The precipitated electron energies were estimated to be higher (>100 keV) than those predicted by ducted gyroresonant interactions and were thus suggested to be consistent with nonducted propagation of NPM signal.

Clilverd and Horne (1996) used ray tracing to show that higher ducting enhancement factors are needed at lower L-shells to keep transmitter signals ducted, implying that ducting should be less frequent at lower L-shells. Predominant nonducted propagation of the NPM and NWC transmitter signals at $L < 1.7$ was confirmed by Clilverd et al. (2008), using statistical wave measurements from the DEMETER (measuring frequencies up to

20 kHz) and CRRES (measuring frequencies of 0.1–400 kHz) spacecraft. However, at $L > 1.7$, little transmitter wave power was detected with frequencies $f > F_{ce0}/2$ for interhemispherically ducted waves, where F_{ce0} is the electron cyclotron frequency at the equator. Thus, the authors argued that the dominant propagation is in ducted mode for VLF transmitter waves at higher L-shells. Preferential ducted propagation at relatively high L-shells was also suggested by Ma et al. (2017) based on statistical analyses of Van Allen Probe observations. The authors have shown that VLF wave power near the magnetic equator decreases significantly at $L \sim 2.5$ for frequencies $f > F_{ce0}/2$ as compared with $f < F_{ce0}/2$. Again, this half-gyrofrequency cutoff is consistent with interhemispheric ducted whistler propagation (Helliwell, 1965; Smith et al., 1960). In addition, based on 10-year statistical wave observations from AKEBONO with frequencies up to ~21 kHz, Agapitov et al. (2014) suggested that the VLF wave power is likely mainly ducted at $L \sim 1.5$–3.

Although it seems most likely that VLF transmitter waves propagate mainly in nonducted mode at low L-shells and primarily in ducted mode at high L-shells, the exact L-shell where the transition to ducted interhemispheric propagation takes place is still unclear. In addition, how much each propagation mode—ducted and unducted—contributes to the net wave power for a specific VLF transmitter is still under debate. For instance, Z. Zhang et al. (2018) combined statistical VLF transmitter wave observations from DEMETER and Van Allen Probes with realistic ray-tracing simulations informed by observations to demonstrate the route of transmitter waves in the magnetospheric meridian plane. Their statistical results suggested that the majority of VLF transmitter signals propagate in a nonducted mode at $L < 3$. Note, however, that statistical spatial distributions of transmitter VLF waves may be insufficient to differentiate ducted and nonducted propagation, because both modes spread over L-shells in the ionosphere due to spreading of signal intensities within the Earth–ionospheric waveguide (Starks et al., 2020; Z. Zhang et al., 2018). A recent study from Gu et al. (2021) has performed a statistical analysis of transmitted WNAs of the Russian Alpha Navigation System (RSDN-20) at the frequency of 11.9 kHz over the L-shell range of 1.8–2.7, based on 6 years of Van Allen Probes wave measurements. The authors found that nonducted propagation dominates (70%) over ducted propagation in both the occurrence and intensity of the observed waves, but that the contribution of ducted signals increases almost linearly with increasing L-shells (from 0% at $L \sim 1.5$ to ~70% at $L \sim 3$). Further taking into account the reduced probability of observing waves with smaller WNA (due to the reduced solid angle sin(WNA), see W. Li, Bortnik, et al., 2013) in statistics from Gu et al. (2021), Ma et al. (2022) showed that the statistical distribution of magnetic wave power from VLF transmitters corresponds to mainly ducted propagation at $L > 1.8$–1.9, in agreement with earlier studies (Agapitov et al., 2014; Clilverd et al., 2008; Ma et al., 2017).

The intensity of VLF transmitter waves is critical for quantifying transmitter-induced energetic electron precipitation. Statistical wave power distributions of transmitter waves in the magnetosphere have been reported by several studies using CRRES, AKEBONO, and Van Allen Probes wave measurements (Agapitov et al., 2014; Clilverd et al., 2008; Ma et al., 2017, 2022; Meredith et al., 2019; Z. Zhang et al., 2018). For example, Ma et al. (2017) have reported statistical transmitter electric field wave power E_w^2 of the order of 10^{-3} $(\mathrm{mV/m})^2$ by averaging Van Allen Probes observations over L-shell, magnetic local time (MLT), Kp, and seasons within a period of 4 years. This globally and statistically averaged VLF wave power has been adopted in quasilinear calculations of the transmitter-driven energetic electron diffusion rates and precipitation over the long term. The quasilinear calculations often result in satisfactory consistency with inner belt observations in terms of long-term dynamics of electron lifetimes and flux variations on the global scales (Albert et al., 2020; Claudepierre et al., 2020; Hua et al., 2020; Ma et al., 2017; Ross et al., 2019; Selesnick et al., 2013). The weak averaged wave power distributed in multibandwidths (≥1 kHz) in general justifies the applicability of the quasilinear diffusion theory to wave–particle interactions due to global VLF transmitter waves (see discussions in Albert, 2001, 2010), although individual VLF stations transmit narrowband emissions with typical bandwidths of ≲200 Hz (Abel & Thorne, 1998; Cohen et al., 2010; Ma et al., 2017).

Meredith et al. (2019) have recently underlined the importance of localized transmitter wave power distributions, that is, in local geographic longitude and for each individual transmitter station, as opposed to statistically and globally averaged wave power as adopted in inner belt models (see, e.g., Ma et al., 2017). Local wave power associated with specific VLF stations during the nighttime has been found to be more than 2 orders of magnitude larger than globally averaged wave power (Meredith et al., 2019; Ross et al., 2019), reaching ~1 mV/m near the longitude of the powerful NWC transmitter (Gamble et al., 2008; Sauvaud et al., 2008; Selesnick et al., 2013). This may correspond to sufficiently strong electron pitch angle diffusion rates to produce significant local BLC electron precipitation, in addition to increasing DLC fluxes as in previous statistical studies (Abel

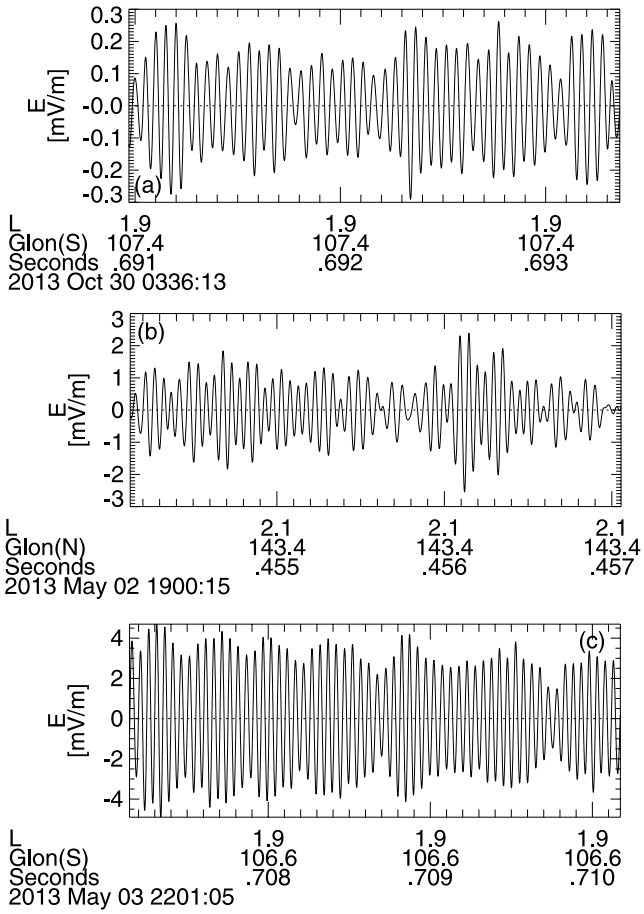

Figure 1. Three examples of waveform measurements of very low frequency (VLF) transmitter waves in the frequency range of 10–30 kHz, as observed by the Van Allen Probes near the equatorial magnetosphere at different times and locations. VLF transmitter wave power occasionally reaches more than 10 $(mV/m)^2$, much higher than the time- and magnetic local time (*MLT*)-averaged transmitter wave power of 10^{-3} $(mV/m)^2$ in 2012–2016 Van Allen Probes statistics (Ma et al., 2017).

& Thorne, 1998; Datlowe & Imhof, 1990; Sauvaud et al., 2008). Figure 1 demonstrates three examples of waveform measurements of large-amplitude VLF transmitter waves performed by Van Allen Probes near the *L*-shells and longitudes where the NWC (L = 1.42, 21.82°S, 114.17°E) and unid25 (L = 1.32, 34.68°N, 126.45°E) VLF transmitter signals are typically reported (Meredith et al., 2019). Figures 1a and 1c show waveform snapshots, both associated with the NWC transmitter for a duration of several milliseconds, which were collected at nearly the same locations but at different universal times. While Figure 1a shows peak wave amplitudes of up to ∼0.2 mV/m, which are roughly 4 times larger than statistically averaged amplitudes (Ma et al., 2017), Figure 1c demonstrates the presence of waves with extremely large peak amplitudes, greater than 4 mV/m, corresponding to a wave power more than 4 orders of magnitude larger than the time-averaged wave power reported by Ma et al. (2017). Similarly, large wave amplitudes of more than 2 mV/m are also seen in Figure 1b, most likely associated with the unid25 transmitter.

Importantly, as wave amplitudes get larger, the applicability of the quasi-linear theory to extremely narrowband VLF transmitter waves becomes doubtful and nonlinear effects of energetic electron scattering may have to be considered (see discussions in Albert, 2002; Karpman, 1974; Shapiro & Sagdeev, 1997; Tao et al., 2012). Thus far, it remains unclear whether local nonlinear wave–particle interactions due to narrowband transmitter waves contribute significantly to inner belt electron precipitation, although it has been well known that relatively long-pulse (>∼100 ms) VLF transmitter waves are often associated with triggered emissions in the magnetosphere, which can only be explained by nonlinear processes (Helliwell, 1965; Helliwell & Katsufrakis, 1974; Nunn, 1974; Omura et al., 1991).

Whether wave–particle interactions occur in a quasilinear regime, or in a nonlinear regime with effects such as phase bunching and phase trapping (Albert et al., 2013; Artemyev et al., 2018; Bortnik et al., 2008; D. R. Shklyar & Matsumoto, 2009), is controlled by the inhomogeneity factor S, the ratio of magnetic field inhomogeneity to the maximum absolute wave amplitude (Bell, 1986; Inan et al., 1978; Karpman et al., 1974; Nunn, 1974; Omura et al., 1991, 2008, 2013). Magnetic field inhomogeneity is a measure of the rate at which an initially resonant particle escapes from resonance due to magnetic gradients along the particle trajectory. If wave amplitudes are high enough with $|S| < 1$, particles can overcome the inhomogeneity and remain trapped for some time (Bell, 1986; Karpman et al., 1974; Nunn, 1974), leading to a breakdown of the unperturbed trajectory approximation assumed in the quasilinear theory of wave–particle interactions (Andronov & Trakhtengerts, 1964; Drummond & Pines, 1962; Kennel & Engelmann, 1966; Vedenov et al., 1962). Note that the condition $|S| < 1$ provides only the minimum wave amplitudes for the activation of nonlinear interactions at a specific location. For nonlinear effects to be important, the wave–particle resonant interaction time duration needs to be larger than the wave trapping period (Artemyev, Neishtadt, Vasiliev, & Mourenas, 2021; Bell, 1986; X.-J. Zhang et al., 2018). Therefore, additional factors such as the coherence length of wave packets and wave amplitude modulations are also important for determining the relative importance of nonlinear scattering compared with quasilinear diffusion (Allanson et al., 2021; An et al., 2022; Gan et al., 2020, 2022; Mourenas et al., 2018; Tao et al., 2013; X.-J. Zhang, Mourenas, et al., 2020; X.-J. Zhang et al., 2018).

Ma et al. (2017) have provided preliminary estimates of the critical wave amplitudes (E_{cr}) of transmitter waves in order for nonlinear energetic electron scattering to take place. It was suggested that for electrons away from the parallel pitch angles, E_{cr} is larger than 0.8 mV/m for L = 2 and energies >100 keV during cyclotron resonances with ducted transmitter waves, and E_{cr} is larger than 3 mV/m for $L < 1.7$ and energies >100 keV during Landau resonance with nonducted waves. Ma et al. (2017) have also argued that the majority (∼90%) of observed VLF waves have average amplitudes of <1 mV/m at L = 2, thus justifying the quasilinear approach for long-term

calculations of electron lifetimes. Note that nonlinear threshold wave amplitudes are much smaller near the equator than off the equator where magnetic field inhomogeneities are larger (Bell, 1986; Bortnik et al., 2008; Omura et al., 2008), but this latitudinal dependence was not included in the above first-order estimates.

On the other hand, given sufficiently large wave amplitudes, nonlinear interactions can still be easily suppressed, or their effects reduced. First, phase decoherence due to short wave packets with phase or frequency variations can effectively detrap resonant particles and reduce the effective duration of nonlinear interaction (X.-J. Zhang, Agapitov, et al., 2020; X.-J. Zhang, Mourenas, et al., 2020; X.-J. Zhang et al., 2018). Second, strong wave amplitude modulations may reduce the efficiency of nonlinear interaction, particularly for phase trapping acceleration (An et al., 2022; Artemyev et al., 2015; Gan et al., 2020; Mourenas et al., 2018; Tao et al., 2013). Third, sideband generations associated with large-amplitude VLF waves or background nonresonant wave fluctuations may disrupt resonant particle coherent trapping, thus prohibiting sustained nonlinear interactions (Artemyev et al., 2015; Brinca, 1980; Dowden, 1982; Karpman, 1974; Nunn, 1986; Omura et al., 1991). These reasons might explain the overall success of quasilinear diffusion theory in accounting for the observed transmitter-induced energetic electron precipitation (Claudepierre et al., 2020; Hua et al., 2020; Selesnick et al., 2013).

However, as recently shown by Claudepierre et al. (2020), the observed inner belt ($L < 2.5$) electron lifetimes are typically more than 1 order of magnitude smaller in observations than in quasilinear calculations. Therefore, the authors suggest that additional loss processes are missing in current models. To fully understand the controlling effect of VLF waves in inner belt electrons losses, we study in this paper the significance of nonlinear effects in transmitter-induced energetic electron scattering and precipitation from the inner belt. Specifically, we shall focus on inner belt wisps and the associated local BLC electron flux increases observed by the ELFIN CubeSats (Angelopoulos et al., 2020). Wisp precipitations at low L-shells ($L \lesssim 2$) are especially interesting, because they are known to be primarily driven by transmitter wave scattering (Sauvaud et al., 2008), enabling us to isolate transmitter wave effects and exclude other scattering contributors such as hiss and lightning-generated whistler waves in the inner belt and slot region (Abel & Thorne, 1998; Albert et al., 2020; Claudepierre et al., 2020).

2. Data and Methodology

We use energetic electron flux measurements from the twin ELFIN CubeSats (ELFIN-A, ELFIN-B; Angelopoulos et al., 2020). Mounted on the spinning ELFIN spacecraft with polar circular orbits at ∼450 km altitude, the energetic particle detector for electrons (EPDE) measures electrons from 50 keV to ∼6 MeV in 16 energy channels with $\Delta E/E \sim 30\%$, and samples the full pitch angle distribution twice in 16 (full-spin) angular sectors with a resolution (FWHM) of ∼22.5° every ∼3 s. Due to limited data downlink budget, EPDE measurements are collected once per radiation belt crossing (i.e., per science zone). During inner belt operations (IBOs), data collections typically last for ∼10 min. During these periods, EPDE operates in integration mode, in which data are averaged over four consecutive spins, resulting in a time resolution of ∼12 s. Nominally, the local magnetic field is within ±15° of the spin plane, allowing ELFIN to reliably resolve the entire electron BLC (spanning ∼62° to ∼72° when calculated at ELFIN altitudes, over all longitudes, and at absolute latitudes of >∼20°). Therefore, in most cases, ELFIN are able to unambiguously measure precipitating, backscattered, and trapped electron fluxes.

We identify wisp events according to their characteristics of narrow, dispersive spectra with energies decreasing with increasing L-shells (Datlowe & Imhof, 1990; Sauvaud et al., 2008). Based on ELFIN observations, we have found two types of wisp events, typically located at $L \leq 2.0$ and $2 < L < 3$, respectively. These double-peak occurrence locations are consistent with statistical distributions of VLF transmitter wave power as reported by Ma et al. (2017) and Meredith et al. (2019). In what follows, we exclusively report wisp events at $L \lesssim 2$ so as to avoid further complexities of untangling transmitter-induced precipitation from other drivers in the slot region, such as hiss and lightning-generated whistlers (Abel & Thorne, 1998). We will focus on wisp precipitation observations by ELFIN during an approximate 1-year period from March 2021 to April 2022. During this period, we have selected 646 ELFIN IBO collections. Within each data collection, ELFIN must have flux measurements within the L-shell range of 1.6–2.1, such that we can reliably identify whether wisp precipitation occurs or not. Consecutive inner belt crossings by ELFIN-A and ELFIN-B within a period of 30 min are regarded as one single data collection.

To obtain a precise knowledge of wisp electron pitch angles, energy-versus-L spectra were obtained for each of the 16 angular sectors. Thus, for each wisp precipitation event, we obtain in total 16 energy-versus-L dispersive

spectra, allowing reliable identification and distinction between DLC and BLC wisp electron fluxes with an angular uncertainty of ~±11.25° (Datlowe & Imhof, 1990; Tu et al., 2010). To avoid spatial or time aliasing, only the eight spectra having a better coverage near the loss cone and recorded within every one half-spin period are kept for further analyses. The IGRF magnetic field model is used to calculate DLCs and BLCs pertinent to ELFIN observations (Alken et al., 2021). In addition, for precipitating or BLC electron fluxes to be considered significant, we require that (a) ELFIN electron fluxes are denoised using an uncertainty threshold of $\Delta J/J \sim 1/\sqrt{N}$ ~70% based on counting statistics, where J is the differential flux and N is the measured count rate; (b) electron loss-cone fluxes are at least 5×10^2/cm^2-s-str-MeV; and (c) the contribution of backscattered electron fluxes from the conjugate region (assumed similar to backscattered fluxes measured in situ) to the measured precipitating fluxes has been subtracted (Mourenas et al., 2021), after which the remaining precipitating fluxes (presumably scattered by the waves) are larger than 10^2/cm^2-s-str-MeV.

Based on the above criteria, we have identified in total 82 clear wisp events, of which 18 events demonstrate detectable BLC electron fluxes within the wisp spectra. Note that only one event showed detectable BLC fluxes but without significant wave-driven precipitation because the criterion (c) was not satisfied. It is also worth emphasizing that in the absence of wave–particle interactions due to transmitter waves and source processes (Abel & Thorne, 1998; Selesnick et al., 2013; Thorne, 2010), there exist little electron fluxes nor wisps in the DLC (electrons are lost in the SAA during each azimuthal drift around the Earth). This low level of quasi-trapped electron fluxes at $L < 2$ has been observed routinely by ELFIN when wisps are not detected. In addition, during eight of our identified wisp events in 2021, the local magnetic field was not at an optimum angle with respect to the spin plane, so that EPDE had limited or even no pitch angle coverage within the BLC, preventing us from identifying whether there was a significant precipitating flux inside the BLC of the wisp.

3. Wisp Precipitation

Figure 2 shows an example of BLC wisp precipitation observed by ELFIN-A during one inner belt crossing in the Northern Hemisphere at the *MLT* of ~1.5 hr on 23 June 2021. Eight energy-versus-L spectra are displayed, corresponding to measurements from eight angular sectors of EPDE. The average pitch angle (α_{avg}), for each angular sector, within four spin periods (~12 s) is indicated. The standard deviations σ_α of pitch angles measured within four spins decrease with increasing pitch angles. For instance, $\sigma_\alpha \sim 4.1°$ for $\alpha_{avg} = 19°$ and $\sigma_\alpha \sim 1.2°$ for $\alpha_{avg} = 50°$. The uncertainty in pitch angle is attributed to the angular half-width of ~11.25°. The local BLC angle is ~67° at ELFIN altitudes of ~450 km and at the longitude of ~172°W in the Northern Hemisphere. Electrons measured by ELFIN at 90° pitch angle have corresponding equatorial pitch angles of 19.9°–23.3° at $L \sim 1.7$–2.0, whereas the corresponding equatorial DLC angles are in the range of 22.5°–28.7° assuming electrons get lost at 100 km altitude in the SAA. Thus, Figures 2a–2c show electron spectra located exclusively within the BLC, Figures 2d–2f show DLC electron spectra, and Figures 2g and 2h show backscattered electron spectra. Note that the above classification of electron fluxes has taken into account the uncertainty of pitch angle measurements, that is, ~11.25°.

Figures 2c–2f reveal narrowband spectra that exhibit energy dispersion with increasing L-shells at $L \sim 1.7$–2.0, a hallmark of transmitter-induced wisp precipitation (Sauvaud et al., 2008). Although the highest wisp electron fluxes are within the DLC, significant precipitating fluxes are also observed in the local BLC as shown in Figures 2a–2c. Electrons within the BLC will precipitate within several bounce periods (several seconds), thus they are most likely to be driven by local transmitter wave scattering. Although previous studies have suggested that most DLC fluxes of wisps are driven by VLF waves associated with the powerful NWC transmitter (Gamble et al., 2008; Sauvaud et al., 2008), the BLC fluxes observed by ELFIN can only be attributed to local transmitters, that is, in this case the NPM station (21.42°N, 158.15°W). This is because the majority of the wave power from individual transmitters is locally confined within ±15° in longitude (Meredith et al., 2019). Similar to the event shown in Figure 2, we have provided in Supporting Information S1 the pitch angle resolved energy-versus-L spectra for the other 17 wisp events with significant BLC fluxes.

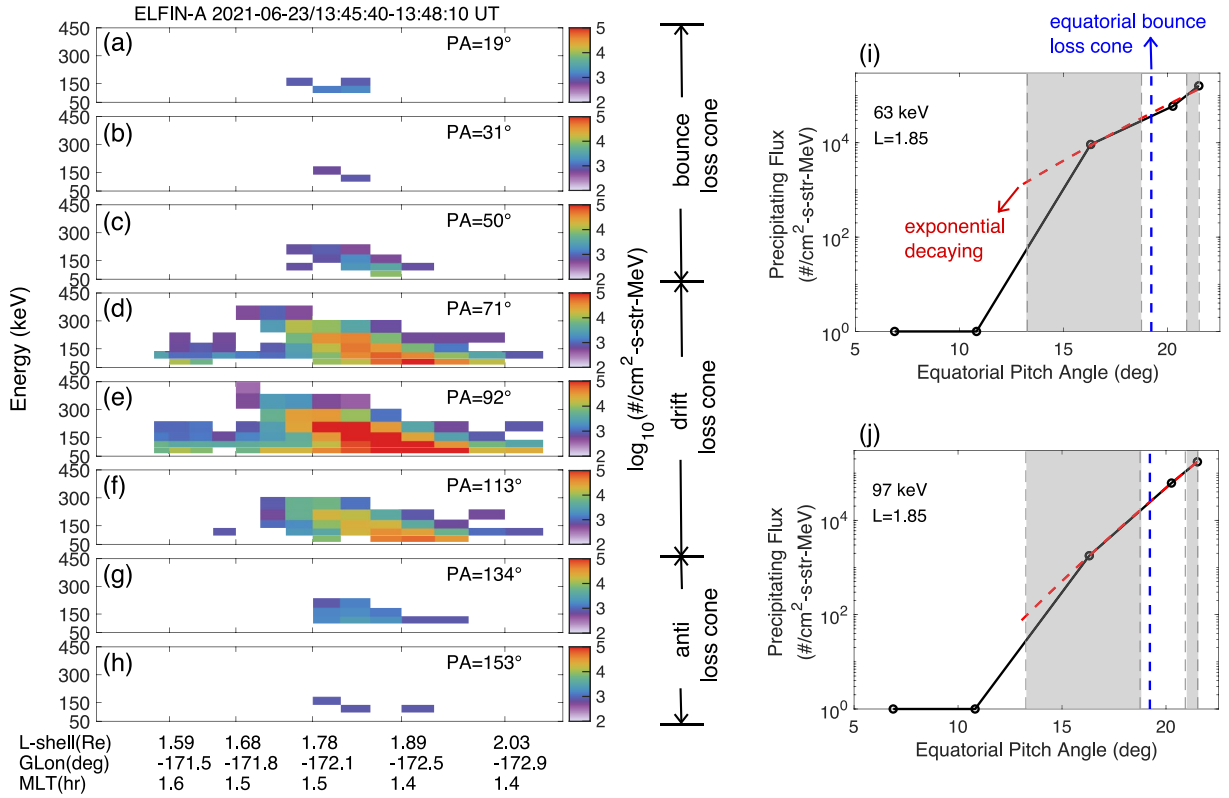

Figure 2. Example of bounce-loss-cone wisp precipitation observed by Electron Loss and Fields Investigation (ELFIN)-A on 23 June 2021 during an inner belt crossing in the Northern Hemisphere. (a–h) Eight energy-versus-L spectra with resolved pitch angles demonstrating both bounce-loss-cone electron measurements (a–c) and drift-loss-cone electron measurements (d–f). (i, j) Precipitating electron equatorial pitch angle distributions measured at 63 keV (i) and 97 keV (j) at $L = 1.85$. The equatorial distributions are obtained by adiabatic mapping from ELFIN altitudes to the equator using the IGRF magnetic field model. An exponentially decaying distribution consistent with the observed distribution is shown as the red dashed lines. The gray shades display the equatorial pitch angle ranges covered by the ELFIN energetic electron detector for electrons measured at the mapped equatorial center pitch angles of 16.3° within the bounce loss cone and 21.5° in the quasi-trapped region. The average equatorial bounce loss cone between the Northern and Southern Hemispheres is 19.2° as indicated by the blue dashed line.

4. Transmitter Wave-Driven Pitch Angle Diffusion Coefficients

Figures 2i and 2j also demonstrate the characteristics of equatorial pitch angle distributions (via adiabatic mapping from ELFIN pitch angle measurements) associated with BLC electrons in Figure 2c. After subtracting the background of backscattered electron fluxes from the conjugate region (Mourenas et al., 2021), we have identified two pixels with significant precipitating fluxes, corresponding to 63 and 97 keV electrons at $L \sim 1.85$, respectively. The pitch angle distributions are roughly consistent with an exponentially decaying function within the loss cone, as shown by the red dashed lines (Kennel & Petschek, 1966). The corresponding equatorial pitch angle extents of electrons measured by the ELFIN EPDE detector at the average local pitch angles of ~50° (or the equatorial pitch angle of 16.3°) and ~90° (or the equatorial pitch angle of 21.5°) are indicated by gray shading. The measurements of full wisp distribution functions allow us to infer the equatorial electron pitch angle diffusion rates based on the quasilinear theory usually assumed to hold for inner belt electron scattering (Abel & Thorne, 1998; Claudepierre et al., 2020; Kennel & Petschek, 1966; W. Li, Ni, et al., 2013; Ma et al., 2017).

Specifically, the flux ratios of 50° (BLC) and 90° (quasi-trapped) electrons measured by ELFIN in this case represent loss-cone filling ratios of scattered electrons from the equatorial magnetosphere (Kennel & Petschek, 1966; W. Li, Ni, et al., 2013). Assuming steady-state quasilinear diffusion equilibrium (this assumption will be discussed later), we may relate precipitating differential fluxes within the equatorial loss cone ($0 < \alpha_{eq} \le \alpha_{LC}$, where $\alpha_{LC} = 19.2°$) to those at the equatorial loss cone angle as (Kennel & Petschek, 1966; W. Li, Ni, et al., 2013; Mourenas et al., 2021; Reidy et al., 2021)

$$J_{eq}(E, \alpha_{eq}) = J_{eq}(E, \alpha_{LC}) \cdot \frac{I_0\left(\frac{\alpha_{eq}}{\alpha_{LC}} Z_0\right)}{I_0(Z_0)}. \quad (1)$$

Precipitating differential fluxes outside the equatorial loss cone ($\alpha_{LC} < \alpha_{eq} \leq 90°$) can be associated with those at the equatorial loss cone as

$$J_{eq}(E, \alpha_{eq}) = J_{eq}(E, \alpha_{LC}) \cdot \left[1 + \ln\left(\frac{\sin \alpha_{eq}}{\sin \alpha_{LC}}\right) \frac{Z_0 I_1(Z_0)}{I_0(Z_0)}\right], \tag{2}$$

where $Z_0 \simeq \alpha_{LC}/\sqrt{D_{\alpha\alpha|LC} \cdot \tau}$ is an energy-dependent parameter defining the diffusion strength at the loss cone, τ is assumed to be a quarter of the bounce period, and I_0 and I_1 are the modified Bessel functions. Assuming adiabatic motion of energetic electrons in the inner belt, the precipitating-over-trapped flux ratios for ~50° and ~90° local pitch angle sectors (Figures 2i and 2j) can be used to derive Z_0 or the quasilinear pitch angle diffusion rate at the equatorial loss cone $D_{\alpha\alpha|LC}$ via (W. Li, Ni, et al., 2013; Reidy et al., 2021)

$$\frac{J_{preci|\sim 50°}}{J_{trapped|\sim 90°}} \simeq \frac{\int_0^{2\pi}\int_0^{\beta} J_{eq}(E, \alpha_{LC}) \frac{I_0\left(\frac{\alpha_{eq}}{\alpha_{LC}} Z_0\right)}{I_0(Z_0)} A \sin\eta d\eta d\psi \Big/ \int_0^{2\pi}\int_0^{\beta} A \sin\eta d\eta d\psi}{\int_0^{2\pi}\int_0^{\beta} J_{eq}(E, \alpha_{LC}) \cdot \left[1 + \ln\left(\frac{\sin \alpha_{eq}}{\sin \alpha_{LC}}\right) \frac{Z_0 I_1(Z_0)}{I_0(Z_0)}\right] A \sin\eta d\eta d\psi \Big/ \int_0^{2\pi}\int_0^{\beta} A \sin\eta d\eta d\psi}, \tag{3}$$

where A is the ELFIN detector area, β is the detector half angle ~11.25°, and η and ψ are related to the precise local pitch angle α of electrons within an elementary solid angle surface area as seen by the ELFIN detector:

$$\cos\alpha = \cos\alpha_{avg} \cos\eta + \sin\alpha_{avg} \sin\eta \cos\psi, \tag{4}$$

with α_{avg} denoting the average angle of the background magnetic field and the detector axis (given by ELFIN data). The equatorial pitch angle α_{eq} is evaluated from the local pitch angle α by $\alpha_{eq} = \sin^{-1}\left[(B_{eq}/B_{ELFIN})^{0.5} \sin\alpha\right]$, where B_{eq} and B_{ELFIN} are the magnetic field intensities measured at the equator and at the ELFIN position. The procedures of the flux ratio calculation and similar definitions of the angle variables can be found in W. Li, Ni, et al. (2013) and their Figure 1. A noted difference in the flux ratio calculation lies in that the measured count rate of the POES detector is integrated in energy, but the ELFIN detector directly measures differential fluxes within small energy steps. Equation 3 can be simplified as

$$\frac{J_{preci|\sim 50°}}{J_{trapped|\sim 90°}} \simeq \frac{\int_0^{2\pi}\int_0^{\beta} J_{eq}(E, \alpha_{LC}) \frac{I_0\left(\frac{\alpha_{eq}}{\alpha_{LC}} Z_0\right)}{I_0(Z_0)} \sin\eta d\eta d\psi}{\int_0^{2\pi}\int_0^{\beta} J_{eq}(E, \alpha_{LC}) \cdot \left[1 + \ln\left(\frac{\sin \alpha_{eq}}{\sin \alpha_{LC}}\right) \frac{Z_0 I_1(Z_0)}{I_0(Z_0)}\right] \sin\eta d\eta d\psi}, \tag{5}$$

where the term $J_{eq}(E, \alpha_{LC})$ cancels for the ratio calculation, and Z_0 is the only unknown parameter which can be calculated numerically. Accordingly, we have obtained the precipitating-over-trapped electron flux ratios of 0.0572 for 63 keV electrons (Figure 2i) and 0.0102 for 97 keV electrons (Figure 2j). These ratios correspond to pitch angle diffusion rates of $D_{\alpha\alpha|LC} \approx 4.9 \times 10^{-3}$ s^{-1} and $D_{\alpha\alpha|LC} \approx 1.5 \times 10^{-3}$ s^{-1}. These quasilinear bounce-averaged diffusion rates in the local precipitation event are more than 3 orders of magnitude larger than drift-averaged diffusion rates calculated from statistical models (Albert et al., 2020; Claudepierre et al., 2020; Ma et al., 2017, 2022; Ross et al., 2019).

The uncertainties of the estimated quasilinear diffusion rates have several sources (Angelopoulos et al., 2020): (a) the uncertainty associated with the measured energies of EPDE detector $\Delta E/E \sim 30\%$, (b) the uncertainty associated with the measured pitch angles of EPDE detector $\Delta\alpha \sim \pm 11.25°$, (c) the uncertainty associated with the measured electron fluxes as determined by counting statistics $\Delta N \sim \sqrt{N}$, where N is the measured count rate, and (d) the uncertainty in measured precipitating flux due to fluctuations in VLF wave power near the equator, which can be estimated as $\Delta J_{preci} \sim \sigma/\sqrt{N_s} \sim 20\%$, with σ the standard deviation of measured fluxes during each spin period and N_s the number of spin periods used for the calculation of the average flux (Mourenas et al., 2021). The uncertainties in detector energy and pitch angle, and the uncertainty in precipitating flux, are the main contributors to the net uncertainty in diffusion rate. A typical ~20% uncertainty in $J_{preci|16.3°}$ in Figures 2i and 2j corresponds to an uncertainty of ~15%–25% in $D_{\alpha\alpha}$. Based on previous analytical results (Albert, 2010; Artemyev et al., 2013), electron bounce-averaged pitch angle diffusion rates for whistlers with small normal angles and for electrons at pitch angles near the loss cone scale with energy as $D_{\alpha\alpha}^{-1} \sim \gamma\left(\gamma^2 - 1\right)^{14/18}\left(\gamma\bar{\omega} - 2\gamma\bar{\omega}^2 + 1\right)(1 - \gamma\bar{\omega})^{4/9}$, where $\bar{\omega} = \omega_m/\Omega_{ce}$, ω_m is the wave center frequency, Ω_{ce} is the electron cyclotron frequency, and γ is the relativistic factor. The diffusion rates scale with pitch angle as $D_{\alpha\alpha} \sim 1/\cos^2\alpha$. Therefore, it is readily

obtained that $\partial D_{\alpha\alpha}^{-1}/\partial\gamma = D_{\alpha\alpha}^{-1}\left[1/\gamma + 14\gamma/9\left(\gamma^2-1\right) + |\bar{\omega} - 2\bar{\omega}^2|/\left(\gamma\bar{\omega} - 2\gamma\bar{\omega}^2 + 1\right) - 4/9\left(1-\gamma\bar{\omega}\right)\right]$ and that $\partial D_{\alpha\alpha}/\partial\alpha = D_{\alpha\alpha} \times 2\tan\alpha$. Then, via error propagation with $d\gamma = dE/m_e c^2$ and $d\alpha = 11.25 \times \pi/180$, we estimate the corresponding uncertainties for 63 keV electrons $u(D_{\alpha\alpha}) \approx 1.5 \times 10^{-3}\ \mathrm{s}^{-1}$ and for 97 keV electrons $u(D_{\alpha\alpha}) \approx 4.9 \times 10^{-4}\ \mathrm{s}^{-1}$.

5. Dispersion Fitting and Wave Normal Angles

Previous studies have revealed that inner belt wisp precipitation is primarily driven by near-equatorial electron pitch angle scattering due to the first-order cyclotron resonance with VLF transmitter waves (Datlowe & Imhof, 1990; Gamble et al., 2008; Sauvaud et al., 2008; Vampola & Kuck, 1978):

$$\omega - k_{\parallel} v_{\parallel} = \Omega_{ce}/\gamma, \tag{6}$$

where ω is the transmitter wave frequency, $k_{\parallel}$ is the parallel wave vector, and $v_{\parallel}$ is the electron parallel resonant velocity. Using the dense plasma ($\omega_{pe} > \Omega_{ce}$) whistler-mode index of refraction $n^2 = c^2k^2/\omega^2 = 1 + \omega_{pe}^2/\omega\left(\Omega_{ce}\cos\theta - \omega\right) \simeq \omega_{pe}^2/\omega\left(\Omega_{ce}\cos\theta - \omega\right)$, we can rewrite Equation 6 to obtain the resonant energy $\gamma = \sqrt{1 + p^2/\left(m_e^2c^2\right)}$, or $(\gamma-1)m_e c^2$ via

$$\frac{\omega}{\Omega_{ce}} + \frac{\cos\alpha\cos\theta}{\sqrt{1 + m_e^2c^2/p^2}}\frac{\omega_{pe}}{\Omega_{ce}}\sqrt{\frac{1}{\Omega_{ce}\cos\theta/\omega - 1}} = \frac{1}{\sqrt{1 + p^2/\left(m_e^2c^2\right)}}, \tag{7}$$

where m_e is the electron mass, c is the speed of light, θ is the transmitter WNA, and Ω_{ce} and the plasma frequency ω_{pe} can be obtained from the IGRF magnetic field model and the plasmaspheric electron density model from Ozhogin et al. (2012). The Ozhogin density model is valid at $L \sim 1.5$–4 and at altitudes greater than 2,000 km, with errors relative to observations of mostly less than 50%, albeit errors higher than 100% have also been reported (Ozhogin et al., 2012).

When the transmitter wave frequencies ω and electron pitch angles α are known from observations, wisp resonant energies depend on variations in WNA θ, magnetic latitude λ (which determines Ω_{ce}), and electron density (or ω_{pe}). Previous studies of wisp dispersion have demonstrated that WNAs control the dispersion slope while electron densities and wave frequencies shift the baseline of the entire resonant energy curve (Datlowe & Imhof, 1990; Imhof et al., 1983). During a single event, ω and ω_{pe} can be considered as constants. Thus, we can infer the VLF transmitter WNAs θ by fitting the observed wisp dispersion with the first-order cyclotron resonance model. This fitting is possible because previous studies have also reported a gradual transition from nonducted to ducted propagation with increasing L-shells for transmitter VLF waves (Agapitov et al., 2014; Clilverd et al., 2008; Gu et al., 2021; Ma et al., 2017; Z. Zhang et al., 2018). Gu et al. (2021) have shown convincing evidence from Van Allen Probe observations of Alpha transmitter wave signals that the average transmitter WNAs decrease linearly at increasing L-shells in a first-order approximation. It is suggested that VLF transmitter waves typically become ducted at $L > 1.8$–1.9 (Clilverd et al., 2008; Ma et al., 2017, 2022). Based on these established results, we next assume monochromatic transmitter waves with linearly decreasing WNAs at increasing L-shells for dispersion fitting of ELFIN-observed wisp spectra.

The procedures for ELFIN-wisp dispersion fitting are (a) we first associate the NWC VLF transmitter station and its wave frequency with the DLC flux increases. We assume that the most powerful NWC station (Meredith et al., 2019) is the main driver of DLC wisp electron scattering at $L \lesssim 2$ as suggested by Sauvaud et al. (2008) and Gamble et al. (2008); (b) starting with nominal plasmaspheric densities based on the Ozhogin et al. (2012) model and assuming equatorial ($\lambda = 0°$) field-aligned transmitter waves, we compare the first-order cyclotron resonant energies as a function of L with wisp dispersion; (c) in the typical case of a mismatch in (b), we specify instead linearly decreasing WNAs θ, and interactively adjust $\theta_{\max}$ and $\theta_{\min}$, which correspond to the minimum and maximum L-shells of the wisp precipitation region, respectively, such that the cyclotron resonant energies as a function of L and the observed wisp dispersion are matched for the slope. Note that $\theta_{\max}$ is constrained by the local Gendrin angle near the equator (Gu et al., 2021; Ma et al., 2022); (d) we then iteratively adjust the equatorial density values within typical uncertainties of <50% of the Ozhogin et al. (2012) model to match the bottom-right corner of the wisp, that is, at the minimum L-shell and the minimum energy of the observed wisp spectrum.

Within this step, the modeled resonant energies at the equator are aligned with the lower edge of the wisp spectrum; (e) to account for the wisp spectral energy width we adjust the latitudinal extent λ_{max}, within which effective wave-induced electron pitch angle scattering takes place, such that off-equator transmitter waves are responsible for scattering of electrons with the resonant energies delineating the upper energy limits of the wisp spectrum. As a result, we have obtained the transmitter WNA distribution in L and an approximate latitudinal range for energetic electron scattering. By trial and error, we find that the uncertainties associated with WNAs θ_{max} and θ_{min} are ∼10°, whereas the uncertainties in λ_{max} are ∼5°. These estimates can be attributed to the measurement resolution in energy and time (i.e., the pixel sizes) during inner belt observations. Note that additional uncertainties may come from variations or spread in frequency of the individual transmitter waves; however, they are very small as mentioned before and modeled resonant energies are much less sensitive to variations in frequency than in latitude.

Because VLF transmitters responsible for local BLC electron fluxes measured by ELFIN may have different wave frequencies from those responsible for DLC fluxes, we also compare the modeled resonant energies with BLC spectra using the local transmitter wave frequency. For simplicity, we assume the same WNA distributions for transmitter waves at the same L-shells. The VLF transmitter stations relevant to inner belt observations ($L \lesssim 2$) are (Meredith et al., 2019) NWC at $L = 1.42$, $lat = 21.82°$S, $lon = 114.17°$E, with a center frequency $f_m = 19.8$ kHz and power of 1 MW; NPM at $L = 1.17$, $lat = 21.42°$N, $lon = 158.15°$W, with $f_m = 21.4$ kHz and power of 600 kW; unid25 at $L = 1.32$, $lat = 34.68°$N, $lon = 126.45°$E, with $f_m = 25.0$ kHz and power of 250 kW; HWU at $L = 1.81$, $lat = 46.71°$N, $lon = 1.24°$E, with $f_m = 18.3$ kHz and power of 200 kW; JJI at $L = 1.25$, $lat = 32.09°$N, $lon = 130.83°$E, with $f_m = 22.2$ kHz and power of 100 kW; ICV at $L = 1.48$, $lat = 40.92°$N, $lon = 9.73°$E, with $f_m = 20.3$ kHz and power of 50 kW; and FTA2 at $L = 1.95$, $lat = 48.54°$N, $lon = 2.58°$E, with $f_m = 20.9$ kHz and power of 50 kW. The VLF station associated with a given BLC wisp precipitation event has been identified only based on its closeness in geographic longitude and L-shell to the wisp observation. The longitudinal range adopted for this identification spans ±∼25° (or slightly more when needed) centered at the longitude of that VLF station. If the BLC wisps are observed at the overlapping longitudes between neighboring stations, the most powerful station is selected as responsible for the BLC wisp event. In principle, transmitter stations with a larger wave power are more influential than those with less power at similar longitudes.

Figure 3 displays an example of wisp dispersion fitting for the event shown in Figure 2. Figures 3a–3c show the background IGRF equatorial magnetic field intensities, equatorial electron densities from the Ozhogin et al. (2012) model, and the ratios of plasma frequencies and electron gyrofrequencies at the equator as a function of L. These parameters are implemented in our resonant energy calculations (Equation 7). Figures 3d–3f present one DLC wisp spectrum and two BLC wisp spectra as already shown in Figures 2e, 2c and 2a. Figure 3d demonstrates that field-aligned ($\theta \sim 0°$) transmitter waves from NWC with a frequency of 19.8 kHz have resonant energies inconsistent with the wisp dispersion slope, as indicated by the black dashed lines. With a WNA θ decreasing linearly from ∼70° to ∼18° at wisp L-shells ($L \sim 1.7$–2.0), the model can well reproduce the observed wisp dispersion for DLC electrons scattered both near the equator ($\lambda \sim 0°$) and off the equator ($\lambda \sim 18°$), as indicated by the solid black and red lines, respectively. For BLC electrons in Figures 3e and 3f, we adopt the local transmitter frequency of 21.4 kHz of the NPM station. The model resonant energies are also consistent with the local precipitating wisp spectrum. Note that we do not rely on dispersion fitting to identify local transmitters associated with BLC wisp precipitation, because variations of resonant energy curves for different VLF transmitter frequencies are almost indistinguishable when compared against ELFIN-observed wisp dispersion. The identification of transmitters associated with local BLC precipitation is solely based on geographic and geomagnetic locations as aforementioned.

6. Statistics of Wisps and Diffusion Coefficients for Locally Precipitating Wisp Electrons

Figure 4a shows the occurrence distribution of ELFIN data collections from 646 inner belt passes during the period of March 2021 to April 2022, along with the measured 64 DLC and 18 BLC wisp events as a function of longitude. Although there are relatively scant orbital passes at certain longitudes, that is, ∼120°–155° and ∼220°–255°, we observe a gradual increase of the occurrences of both DLC and BLC wisps from the east side of the SAA and the occurrences peak near ∼170°–200°. This global wisp distribution is in general agreement with previous wisp statistics measured by DEMETER (Sauvaud et al., 2008; Gamble et al., 2008; X. Li et al., 2012),

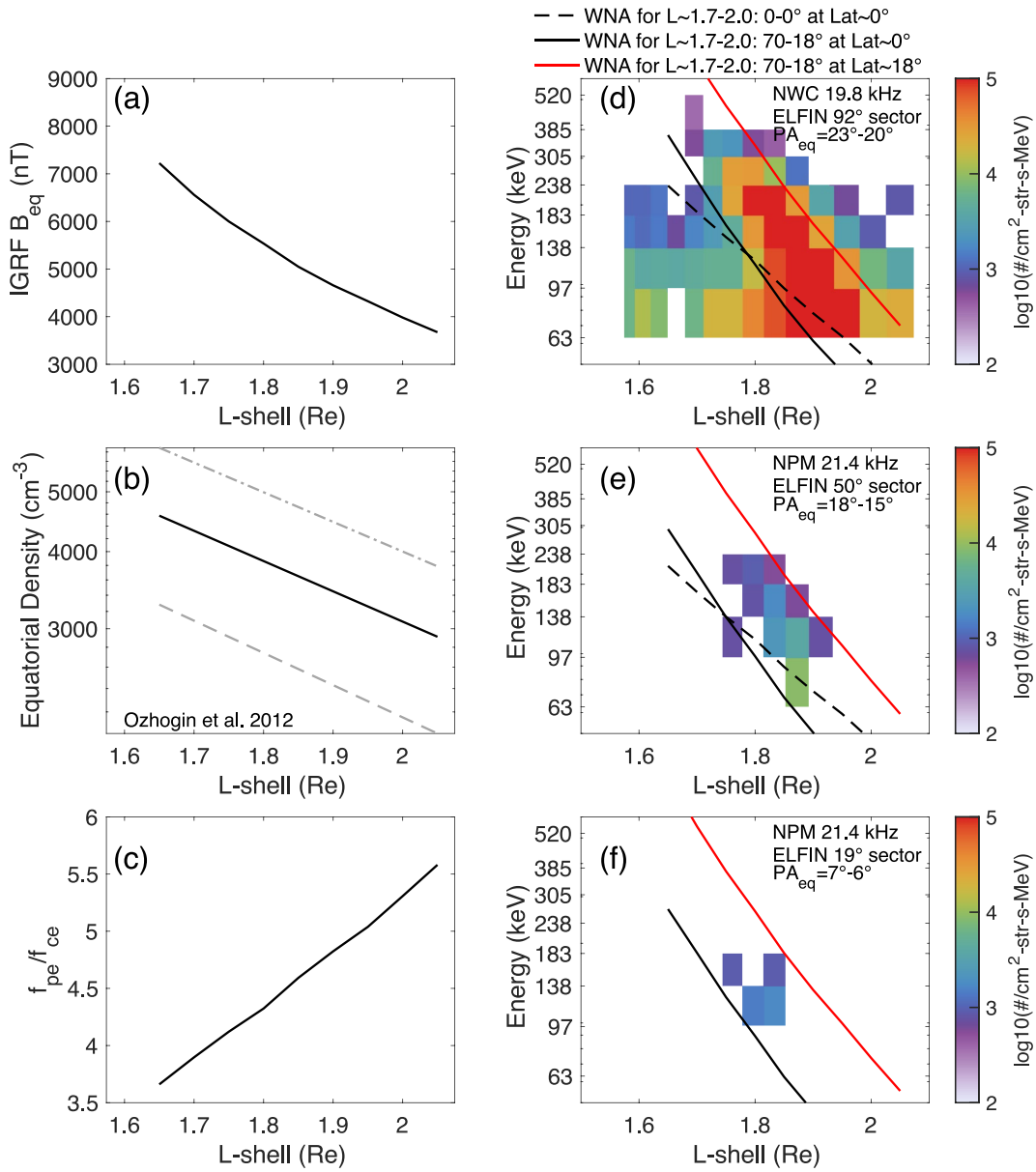

Figure 3. Example of applying the first-order cyclotron resonance model to dispersive wisp spectra fitting for the event shown in Figure 2. This fitting aims to infer wave normal angles and latitudinal distributions of transmitter waves associated with Electron Loss and Fields Investigation (ELFIN) observations. (a–c) IGRF equatorial magnetic field intensities, Ozhogin et al. (2012) plasmaspheric equatorial densities, and the corresponding ratios of the plasma frequency (f_{pe}) over the electron gyrofrequency (f_{ce}) as a function of L-shells. (d) Drift-loss-cone wisp spectra measured at pitch angles of ~90°. The black dashed line indicates the modeled resonant energies assuming field-aligned transmitter waves and a frequency of 19.8 kHz related to NWC. The black and red solid lines indicate modeled resonant energies at the equator and off the equator ($\lambda = 18°$), assuming linearly decreasing wave normal angles from 70° to 18° within $L = 1.7$–2.0. (e, f) Bounce-loss-cone wisp spectra measured at pitch angles of ~50° and ~19°. The corresponding mapped equatorial pitch angles (PA_{eq}) are also indicated. The modeled resonant energies shown in black and red solid lines assume again linearly decreasing wave normal angles but with a frequency of 21.4 kHz corresponding to the local NPM transmitter.

with the distinction that DEMETER was located at altitudes of ~700 km, whereas ELFIN were positioned at altitudes of ~450 km. Figure 4b displays the corresponding BLC wisp precipitation occurrence rate as a function of longitude. The occurrence rate reaches up to ~20% relative to ELFIN inner belt observations at a specific longitude. It is emphasized that although the occurrence rate is maximum near 120° longitude where the NWC station resides nearby, the data coverage at this position is poor (one wisp out of five orbits). The broad peak of

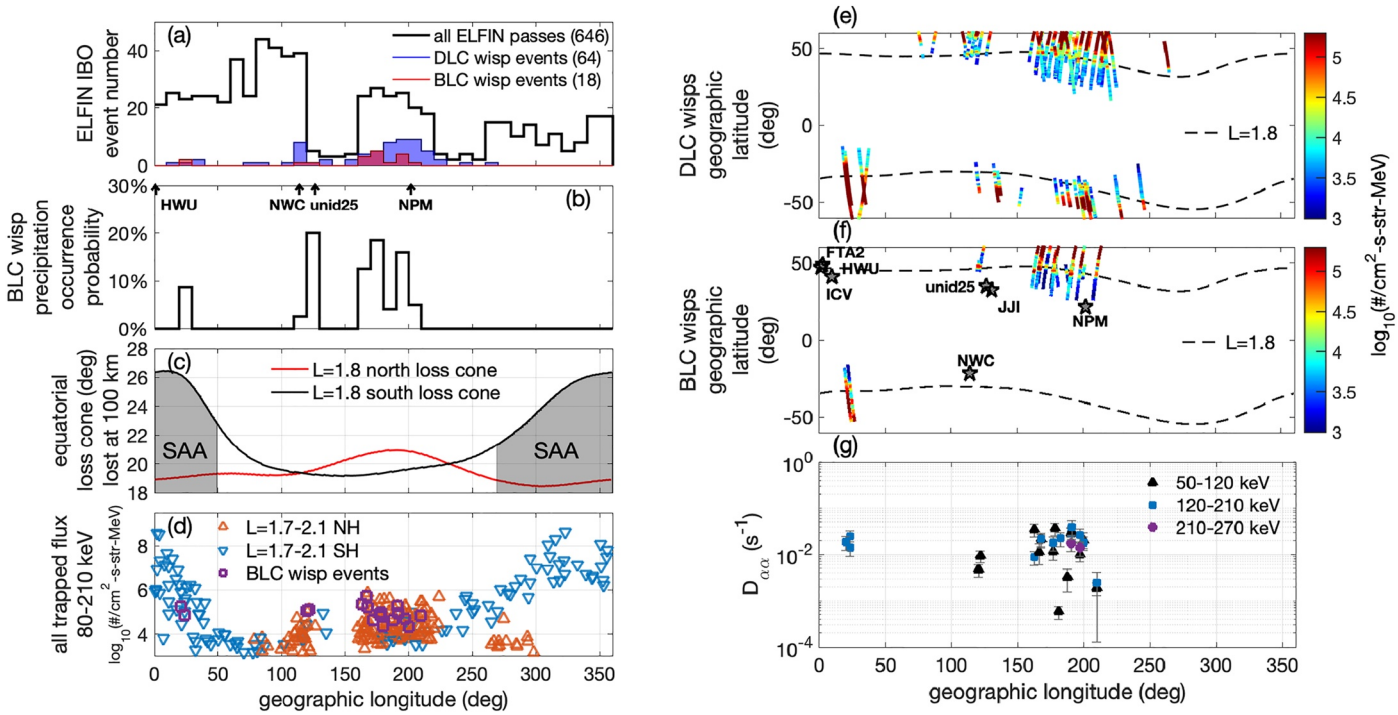

Figure 4. (a) Distribution of Electron Loss and Fields Investigation (ELFIN) inner belt operation orbital passes (black histogram), drift-loss-cone (DLC) wisp events (blue filled histogram), local bounce-loss-cone (BLC) wisp precipitation events (red filled histogram) as a function of longitude as measured during the period of March 2021 to April 2022. (b) Occurrence probability of BLC wisp events relative to all ELFIN inner belt operations (IBOs) as a function of longitude. The most powerful four stations located at $L \lesssim 2$, that is, NWC, NPM, unid25, and HWU, have been indicated by black arrows. (c) Equatorial BLCs corresponding to the Northern (red) and Southern (black) Hemispheres as a function of longitude. The South Atlantic Anomaly (SAA) region is indicated by gray shading. (d) Maximum trapped electron fluxes measured at ∼90° pitch angle in $L \sim 1.7$–2.1 and averaged over the energy range of 80–210 keV as a function of longitude. Only the 265 events with trapped fluxes larger than 10^3/cm^2-s-str-MeV are displayed. Fluxes measured at the Northern and Southern Hemispheres are indicated by the orange upward-facing triangles and blue downward-facing triangles, respectively. Trapped fluxes measured during BLC wisp precipitation events are highlighted by purple squares. (e) Flux distributions along ELFIN orbits for wisp events when only DLC electrons were observed. (f) Flux distributions along ELFIN orbits for wisp events when BLC electrons were measured. The very low frequency (VLF) stations relevant to the inner belt wisps at $L \lesssim 2$ are also displayed. (g) Inferred quasilinear diffusion rates based on the measured precipitating-over-trapped flux ratios for 17 BLC wisp events when significant precipitating fluxes were observed. The BLC electron energies are grouped according to the ELFIN electron detector energy channel widths of 50–120 keV, 120–210 keV, and 210–270 keV, with uncertainties associated with individual data points shown by error bars.

occurrence rate at ∼170°–200° corresponds to the location of the NPM transmitter, although some BLC wisps are observed at ∼170°, up to ∼35° away from the longitude of NPM. This broad peak of BLC wisp occurrence rate is consistent with statistical results from the Van Allen Probes (see Figure 4d from Meredith et al., 2019), which indicate that the nightside average transmitter wave power at 21.03–22.07 kHz (the frequency range of NPM) and $L \sim 1.8$ actually remains elevated (i.e., higher than one third of the NPM peak power found at ∼200°) over the whole 120°–220° longitudinal domain, probably as a result of superposition with other waves originating from transmitters JJI, unid25, and NWC. This suggests that the BLC wisps observed near 170° could be due to an occasional superposition of relatively intense waves coming from several of these transmitters (Gu et al., 2021; Thorne & Horne, 1994). The overall occurrence rate of BLC wisp precipitation events relative to all ELFIN inner belt observations is 18/646 ≃ 3%. This low occurrence rate is consistent with statistical observations of VLF transmitter waves in the magnetosphere, which indicate that high-intensity transmitter waves with full amplitudes of >∼1 mV/m are recorded only a few percent of the time (Abel & Thorne, 1998; Ma et al., 2017; Meredith et al., 2019).

Figure 4c shows typical equatorial BLCs corresponding to the Northern and Southern Hemispheres at $L \sim 1.8$. The equatorial DLC range can be inferred by the difference between the minimum (∼19°) and maximum (∼26.5°) BLCs in longitude. The SAA geographic longitudes (to the west of 50° and to the east of 270°) are indicated by the gray shading. Figure 4d provides the maximum trapped flux distribution in longitude from 265 ELFIN inner belt passes when the measured fluxes exceed the threshold of 10^3/cm^2-s-str-MeV at the ∼90° pitch angle sector

within $L \sim 1.7$–2.1. Trapped fluxes measured in the Southern Hemisphere (blue downward triangles) maximize in the SAA region. Trapped fluxes in the local hemisphere are generally larger than those in the conjugate hemisphere when the corresponding equatorial BLCs are larger, and vice versa; the trapped flux level varies proportionally to the corresponding equatorial loss cone size (Figure 4c). The majority of the observed local BLC wisp precipitating events (purple squares) are located in the Northern Hemisphere near the longitudes of ∼160°–200° where the corresponding loss cone angles are largest eastward of the SAA region. Locally, BLC wisp precipitation events occurring far from the SAA correspond to stronger trapped fluxes than events without a signature of BLC wisp precipitation, although there is also an important dependence on *MLT* (see below). Figures 4e and 4f further display the trapped flux distribution in geographic latitude (or equivalently in L) for DLC and BLC wisp precipitation events, respectively. ELFIN measurements were averaged over the 80–210 keV energy range. Local maxima of wisp fluxes near $L \sim 1.8$ can be identified clearly east of ∼110° longitude for both DLC and BLC wisp events, the latter of which showing stronger wisp electron fluxes. The gradual flux increase eastward of the SAA can also be identified in Figure 4e for DLC wisp events.

Two important features of BLC wisp precipitating events in Figure 4f are worth emphasizing here. First, except for the two events observed near the eastward edge of the SAA in the south, the majority of BLC wisps are observed in the Northern Hemisphere. This result is statistically significant because there have been a number of wisps observed with only DLC fluxes in the Southern Hemisphere. The preferential occurrence of BLC wisp precipitation events in the Northern Hemisphere can be explained by the larger local BLCs at geographic longitudes of 150°–230° as shown in Figure 4c. The narrower BLC in the Southern Hemisphere than in the Northern Hemisphere at similar altitudes corresponds to lower trapped fluxes and consequently lower BLC fluxes, less easily measurable by ELFIN. In addition, all VLF transmitters are located in the north, except for NWC. As a result, electrons precipitating in the north can interact near the equator via first-order cyclotron resonance with intense waves directly coming from northern VLF transmitters, whereas electrons precipitating in the south can interact with waves from northern transmitters only after they have been partly reflected by the ionosphere and crossed again the equator with reduced amplitudes. Therefore, BLC precipitation in the north is expected to be stronger near northern transmitters than near the southern NWC transmitter.

Second, only two BLC wisp precipitation events were observed to be associated with the most powerful NWC station, and most BLC wisps were measured further eastward, most likely associated with the NPM station. This is in contrast to the conclusions made by previous studies that the NWC station is probably most important for scattering wisp energetic electrons from the inner belt (X. Li et al., 2012; Sauvaud et al., 2008). Fewer local BLC wisps were observed near NWC longitudes, because there was only little trapped electron flux at such longitudes near the edge of the SAA region where most electrons have already been lost into the atmosphere, making it harder for waves to scatter significant fluxes into the local BLC near NWC. Moreover, electrons can be precipitated in the north by NWC waves only if these waves have already been reflected at least once and probably lost some power. Waves emitted by NWC can directly interact only with electrons precipitating in the south, where the BLC is narrower than in the north at longitudes 115°–130° just eastward from NWC, corresponding to even lower trapped fluxes than in the north (as shown by the presence of only rare blue triangles in this region in Figure 4d). However, trapped electron fluxes increase as the longitudinal distance from the SAA increases, as clearly demonstrated in Figure 4d. This increase of trapped flux is due to (a) the time needed for pitch angle diffusion to replenish the pitch angle range of quasi-trapped electrons along the azimuthal drift of electrons toward the east and (b) the gradual increase of the local BLC further eastward as shown in Figure 4c. Insufficient orbital coverage immediately to the east of the NWC station may also affect the wisp occurrence estimation. As a result, most BLC wisp precipitation events observed by ELFIN are located away from, and to the east of, the NWC station and their occurrence rate peaks near the longitudes of the NPM station. In fact, Sauvaud et al. (2008) have also measured stronger DLC fluxes near NPM longitudes in the Northern Hemisphere compared with those near the NWC station (see their Figure 2).

For each wisp event with significant wave-driven precipitating fluxes within the BLC (17 events), we can infer the corresponding electron pitch angle diffusion coefficients, as detailed in the previous section. Figure 4g displays the transmitter-induced energetic electron pitch angle diffusion rates $D_{\alpha\alpha}$ versus longitude as inferred from the corresponding BLC wisp events. The diffusion rates have been calculated separately for different energy channels during each event as described in Section 4. Here, we group the obtained $D_{\alpha\alpha}$ values during each event into three energy ranges of 50–120 keV, 120–210 keV, and 210–270 keV, with the uncertainty $u(D_{\alpha\alpha})$ determined either by the largest uncertainty associated with individual diffusion rates (see details in Section 4) or

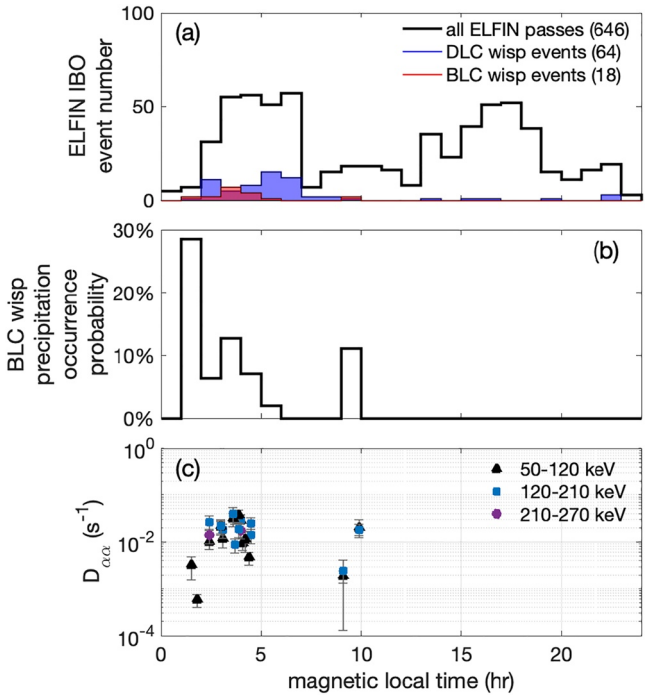

Figure 5. (a) Distribution of Electron Loss and Fields Investigation (ELFIN) inner belt operation orbital passes (black histogram), drift-loss-cone (DLC) wisp events (blue filled histogram), and local bounce-loss-cone (BLC) wisp precipitation events (red filled histogram) as a function of magnetic local time (*MLT*) as measured during the period of March 2021 to April 2022. (b) Occurrence probability of BLC wisp events relative to all the orbital passes as a function of *MLT*. (c) Inferred quasilinear diffusion rates versus *MLT* in the same format as in Figure 4g.

by the standard deviation of the grouped diffusion rates themselves, whichever is larger. The obtained transmitter-induced $D_{\alpha\alpha}$ are on the order of 10^{-4} to 10^{-2} s^{-1}, nearly 4 orders of magnitudes larger than statistical diffusion rates calculated using time-, *MLT*-, and longitude-averaged transmitter wave power (Albert et al., 2020; Claudepierre et al., 2020; Hua et al., 2020; Ma et al., 2017; Ross et al., 2019; Selesnick et al., 2013). The majority of the wisp precipitation events were observed within ±25° longitude with respect to the four powerful inner belt transmitter stations of NPM, NWC, unid25, and HWU (Meredith et al., 2019), although several events were located more than 30° in longitude away from any of these transmitters.

Figure 5 shows additionally the occurrence distribution of the 646 ELFIN IBOs and the measured DLC and BLC wisp events as a function of *MLT*. Figure 5b indicates that BLC wisp precipitation events are mainly observed in the 1–6 hr *MLT* sector, with an average occurrence rate of ∼10% there (at 1–2 hr in *MLT*, the occurrence rate of over 25% is partly due to poor statistics in this sector). Figure 5a also shows that the majority of the wisp events are located in the morning sector at ∼1–7 hr *MLT*. These results are consistent with the average VLF transmitter wave power distribution, which similarly peaks at *MLT* of ∼1–6 hr as reported by Ma et al. (2017) using Van Allen Probe observations.

For all wisp events, we can infer transmitter WNAs based on wisp spectral dispersion fitting as outlined in the previous two sections. Here, we only perform this wave normal inference for the 17 events with significant precipitating fluxes after subtracting the backscattered flux. We have provided in Table S1 in Supporting Information S1 detailed information on UT, geomagnetic and geographic locations, background field and plasma parameters, derived transmitter wave characteristics, energetic electron energies, pitch angles and flux ratios, and the associated diffusion coefficients for loss-cone electrons of the BLC wisps measured by ELFIN.

7. Transmitter Wave Amplitudes and Nonlinear Thresholds

We have shown that the quasilinear electron pitch angle diffusion rates of wisps estimated from in situ ELFIN measurements are several orders of magnitude larger than diffusion rates previously reported in statistical quasilinear models (Albert et al., 2020; Claudepierre et al., 2020; Hua et al., 2020; Ma et al., 2017; Ross et al., 2019; Selesnick et al., 2013). This finding begs the question whether nonlinear effects need to be considered to explain very fast electron scattering, corresponding to the exceedingly large inferred diffusion rates and the associated local BLC precipitation events. According to quasilinear theory (Kennel & Engelmann, 1966), electron pitch angle diffusion rates scale linearly with whistler-mode wave power. Therefore, we can infer quasilinear wave power or amplitudes based on the diffusion rates obtained from ELFIN measurements (W. Li, Ni, et al., 2013; Ni et al., 2014). Such inferred amplitudes can be compared with the critical threshold wave amplitude E_{cr} in order to check whether nonlinear interactions may take place (Bell, 1986; Karpman, 1974; Omura et al., 1991, 2008; X.-J. Zhang et al., 2018). If $E_w < E_{cr}$, the wave amplitude effect is weaker than the magnetic field inhomogeneity effect which leads to random wave phases as seen by the resonant particles, thus justifying the quasilinear treatment; if $E_w > E_{cr}$, peak wave amplitudes are strong enough to overcome the magnetic field inhomogeneity effect and potentially produce nonlinear phase bunching or phase trapping (Albert et al., 2013; Bell, 1986; Karpman & Shklyar, 1977; D. R. Shklyar & Matsumoto, 2009).

To estimate the wave amplitude associated with the quasilinear electron pitch angle diffusion rate $D_{\alpha\alpha}$ obtained from ELFIN measurements, we will first calculate normalized bounce-averaged pitch angle diffusion rates $D_{\alpha\alpha|\,\mathrm{norm}}$ for loss-cone electrons, given a nominal, reference transmitter full wave amplitude $B_{w0} = 1$ pT. Assuming quasilinear pitch angle scattering, we can estimate wave amplitudes as $B_w = B_{w0}\sqrt{D_{\alpha\alpha}/D_{\alpha\alpha|\mathrm{norm}}}$. Here, $D_{\alpha\alpha|\,\mathrm{norm}}$ is calculated under the following conditions: (a) the background magnetic field, geographic, and geomagnetic locations are consistent with those used for deriving $D_{\alpha\alpha}$ based on ELFIN measurements; (b) the local transmitter

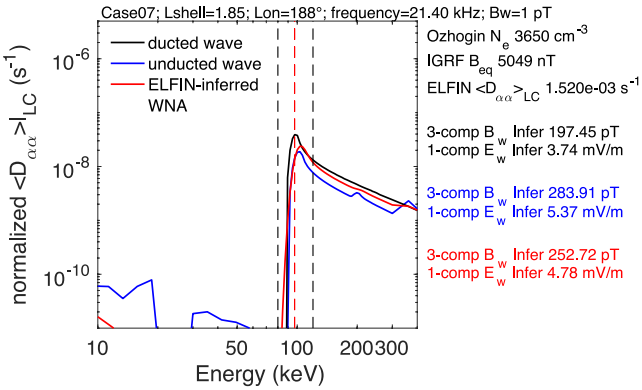

Figure 6. Normalized quasilinear electron pitch angle diffusion coefficients at the loss cone as a function of energy, assuming NPM transmitter waves with a center frequency of 21.4 kHz, a full wave amplitude of B_{w0} of 1 pT, at positions pertinent to observations in Figure 2j. This example is associated with wisp precipitating electrons observed in the 97 keV channel of Electron Loss and Fields Investigation (ELFIN) energetic particle detector for electrons (EPDE) during the event on 23 June 2021. The corresponding energy channel width is delineated by the two vertical black dashed lines, whereas the center energy of 97 keV is shown as the vertical red dashed line. The associated background parameters and inferred wave amplitudes are also indicated. The numerical calculations are performed for very low frequency (VLF) transmitter waves in ducted mode (black solid curve), in nonducted mode (blue solid curve) with a wave normal angle model from Gu et al. (2021), and with wave normal angles obtained from ELFIN-wisp dispersion fitting (red solid curve). The inferred full wave amplitude B_w and the one-component amplitude E_w for different models are indicated by the corresponding colored notations.

frequencies are centered at the frequency f_m with the lower and upper cutoff frequencies of $f_m \pm 1$ kHz; (c) the transmitter WNA model is taken as a Gaussian with a mean θ_m obtained by ELFIN-wisp dispersion fitting (as provided in Table S1 in Supporting Information S1), a width $\theta_w = 10°$, a minimum $\theta_{\min} = 0°$, and a maximum $\theta_{\max} \sim \theta_m + 10°$ while restricted by the Gendrin angle (Ma et al., 2022). For comparison with previous statistical models, we perform additional calculations of diffusion rates using a ducted transmitter wave model with $\theta_m = \theta_{\min} = 0°$, $\theta_w = 10°$, and $\theta_{\max} = 30°$, and using a nonducted transmitter wave model (Ma et al., 2022) with θ_m close to 60°, as informed by recent Van Allen Probe statistical measurements from Gu et al. (2021).

To generate peak diffusion coefficients consistent with ELFIN-wisp observations, we adjust the model equatorial densities such that the first-order cyclotron resonant energies are consistent with those of the measured wisp electrons within the energy channel width of the ELFIN EPDE detector. The density adjustments are typically within 50% deviations from the nominal values predicted by Ozhogin et al. (2012). Also, the inferred transmitter wave full magnetic field amplitude B_w is used to derive the wave full electric field amplitude using the whistler-mode dispersion relation (Ma et al., 2017; Ni et al., 2011). The full electric field amplitudes are then divided by $\sqrt{3}$ to obtain the one-component electric field amplitudes of VLF transmitter waves, which are typically measured by spacecraft at frequencies higher than 10 kHz (Agapitov et al., 2014; Clilverd et al., 2008; Ma et al., 2017).

Figure 6 shows one example of calculated normalized bounce-averaged pitch angle diffusion rates as a function of energy for electrons near the loss cone under the influence of transmitter waves with the reference amplitude $B_{w0} = 1$ pT and using three different WNA models as aforementioned. The bounce-averaged pitch angle diffusion rate estimated from ELFIN is 1.52×10^{-3} s^{-1}. This information is indicated in Figure 6 along with the background parameters and the inferred wave amplitudes under the three WNA models, that is, ducted (black solid curve), nonducted (blue solid curve), and ELFIN inferred (red solid curve). In this case, the normalized diffusion rates for the three models are very similar, peaking near the resonant energy of 100 keV with peak $D_{\alpha\alpha|\,\mathrm{norm}}$ on the order of 10^{-8} s^{-1}. The ELFIN-inferred WNA model has a mean $\theta \sim 44°$, thus the corresponding $D_{\alpha\alpha|\,\mathrm{norm}}$ is more aligned with the diffusion rates in the ducted mode. The same conclusion can be drawn for the majority of our BLC wisp precipitation events (Table S1 in Supporting Information S1). Note that the two peaks in $D_{\alpha\alpha|\,\mathrm{norm}}$ away from 100 keV for the nonducted model are due to higher-order cyclotron resonances with oblique transmitter waves (Artemyev et al., 2016; Ma et al., 2022). Using the ELFIN-inferred θ in our individual wisp event, we have obtained a one-component wave electric field of ~4.8 mV/m. Such a level of VLF transmitter wave amplitude is realistic, since it has already been observed by the Van Allen Probes near the equator, as in one example shown in Figure 1. Based on low-altitude wave measurements by DEMETER, the average nighttime wave amplitude near the equator close to the NWC transmitter has been estimated to be of a similar magnitude, ~0.5–1 mV/m, although sensibly smaller (Gamble et al., 2008; Sauvaud et al., 2008; Selesnick et al., 2013). Applying similar procedures, we have estimated the corresponding quasilinear wave electric field amplitudes for the local BLC wisp precipitation events as listed in Table S1 in Supporting Information S1.

The nonlinear threshold wave amplitudes E_{cr} are estimated based on the inhomogeneity factor S, which is a ratio between magnetic field inhomogeneity (i.e., the inertial and mirror forces) and the wave electromagnetic forces (Karpman et al., 1974; Nunn, 1974; Omura et al., 2008). When $|S| < 1$, nonlinear wave–particle interactions such as phase bunching or trapping may take place for resonant electrons. The formula of S has been provided by Omura et al. (2008):

$$S = -\frac{1}{\omega_t^2 \delta^2}\left[\gamma\left(1-\frac{V_R}{V_g}\right)\frac{\partial\omega}{\partial t} + \left[\frac{k\gamma v_\perp^2}{2\Omega_{ce}} - \left(1+\frac{\delta^2}{2}\frac{\Omega_{ce}-\gamma\omega}{\Omega_{ce}-\omega}\right)V_R\right]\frac{\partial\Omega_{ce}}{\partial h}\right], \quad (8)$$

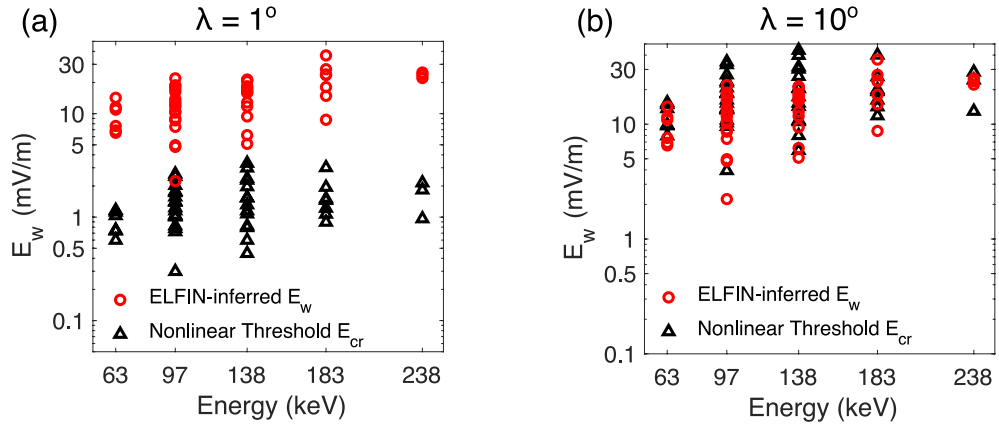

Figure 7. Comparisons of Electron Loss and Fields Investigation (ELFIN)-inferred very low frequency (VLF) transmitter wave electric field amplitudes E_w (red circles) using the quasilinear theory and nonlinear threshold electric field amplitudes (black triangles) predicted by the inhomogeneity factor S (Omura et al., 2008). (a) One-component ELFIN-inferred transmitter wave electric field amplitudes and nonlinear threshold amplitudes as a function of energy at $\lambda = 1°$. (b) One-component ELFIN-inferred transmitter wave electric field amplitudes and nonlinear threshold amplitudes as a function of energy at $\lambda = 10°$.

where $\omega_t = \sqrt{kv_\perp \Omega_{ce} B_w / B_0}$, B_0 is the background magnetic field intensity, $\delta = 1 - \omega^2/c^2k^2$, and V_R and V_g are the resonant electron phase velocity and group velocity, respectively. The frequency variation $\partial\omega/\partial t$ can be ignored for VLF transmitter waves. The S parameter depends on electron energy and pitch angle as well as on latitude, which dictates the variation in $\partial\Omega_{ce}/\partial h$ along the field line. Using the dipole magnetic field, we obtain the following expression for E_{cr} under the condition $S = 1$:

$$E_{cr} = \frac{cB_0}{\delta^2}\left\{-\frac{c\sqrt{\gamma^2-1}\sin\alpha}{2\Omega_{ce}} + \left(1-\delta^2\right)\frac{\left[1+\delta^2\dfrac{\Omega_{ce}-\gamma\omega}{2\left(\Omega_{ce}-\omega\right)}\right]c\left(\Omega_{ce}-\gamma\omega\right)}{\omega^2\sqrt{\gamma^2-1}\sin\alpha}\right\}\times \frac{3\sin\lambda}{LR_E}\left[\frac{3+5\sin^2\lambda}{\cos^2\lambda\left(1+3\sin^2\lambda\right)^{1.5}}\right], \quad (9)$$

where R_E is the Earth's radius. It is noted that ELFIN-measured electron energies have an uncertainty of $\Delta E \sim 30\%E$, which is comparable with the energy spread due to wave–particle resonances within a latitudinal extent of ~10° near the equator. Therefore, it is expected that resonant interactions within a range of latitudes near the equator may all contribute to precipitation within one energy channel measured by ELFIN. Here in Equation 9, we only use the average energy of each measurement for calculations at different resonance latitudes near the equator.

The full wave electric field threshold amplitudes are then divided by $\sqrt{3}$ for comparison with the above one-component E_w estimated in the same way based on full amplitudes inferred from ELFIN-wisp measurements. Figure 7 demonstrates such comparisons as a function of energy at latitudes close to the equator with $\lambda = 1°$ (Figure 7a) and slightly off the equator with $\lambda = 10°$ (Figure 7b). The ELFIN-inferred one-component wave electric field amplitudes E_w are in the range of 1–30 mV/m, whereas the corresponding threshold E_{cr} for nonlinear interactions of near-loss-cone electrons are in the range of 0.1–3 mV/m at $\lambda = 1°$. At $\lambda = 10°$, E_{cr} values are slightly larger than ELFIN-inferred E_w. Therefore, in terms of wave intensities, nonlinear effects need to be considered for resonant electrons interacting with VLF transmitter waves near the equator at latitudes $\lambda \leq$ ~10°, at least for the BLC wisp precipitation events measured by ELFIN.

8. Discussion

Based on ELFIN observations of inner belt wisp full electron pitch angle distributions, we have estimated the bounce-averaged pitch angle diffusion coefficients for wisp precipitation events with significant BLC fluxes, assuming steady-state quasilinear diffusion equilibrium (Kennel & Petschek, 1966; W. Li, Ni, et al., 2013; Mourenas et al., 2021; Reidy et al., 2021). Such an assumption is usually valid for inner belt energetic (50–500 keV) electrons, with lifetimes typically on the order of days to months (Claudepierre et al., 2020). However, exceedingly large diffusion coefficients on the order of 10^{-4} to 10^{-2} s^{-1} have been obtained in our strong wisp precipitation events, compared with typical drift-averaged diffusion rates of up to 10^{-6} s^{-1} based on global statistical averages of transmitter wave models (Albert et al., 2020; Claudepierre et al., 2020; Ma et al., 2017, 2022; Ross et al., 2019; Selesnick et al., 2013). Accordingly, the discrepancy between the inferred wave power during strong BLC precipitation events and the time- and *MLT*-averaged wave power is about a factor of $\sim 10^2$ to 10^4.

Part of this discrepancy can be ascribed to the much higher wave power present within $\pm 10°$ of the longitude of a given transmitter, and to the much higher wave power at 1–6 *MLT* due to lower wave absorption (Gamble et al., 2008; Ma et al., 2017; Meredith et al., 2019; Sauvaud et al., 2008; Selesnick et al., 2013; Starks et al., 2020), corresponding to a factor $\sim 10^2$ increase in wave power at 1–6 *MLT* near a given transmitter compared to the time- and *MLT*-averaged power. Part of the remaining discrepancy—that is, a factor $\sim 1-10^2$ augmentation of wave power during strong BLC wisp events compared to average power at 1–6 *MLT* within $\pm 10°$ of a transmitter—may be explained by larger-amplitude transmitter waves occasionally observed in the magnetosphere (e.g., see Figure 1; VLF transmitter wave power occasionally exceeds 10 $(mV/m)^2$), probably due to ray merging (Gu et al., 2021; D. R. Shklyar & Jiříček, 2000; Thorne & Horne, 1994), local wave amplification through wave–particle interactions (Omura et al., 2008; D. Shklyar & Luzhkovskiy, 2022), or through coupling with local ionospheric disturbances (Cohen et al., 2010). In this regard, it is important to emphasize that the majority of wisps observed by ELFIN are only recorded within the DLC. The local occurrence rate of BLC precipitation events (with respect to all ELFIN measurements) at longitudes within $\pm 20°$ of the NPM transmitter and 1–6 *MLT* is $\sim 11\%$ based on ELFIN statistics in Figures 4 and 5. This local occurrence rate is consistent with an additional increase by a factor of ~4–5 of transmitter wave power, at a given time and location, during the strong BLC wisp precipitation events used to infer the wave power.

As a result, the remaining discrepancy between inferred and expected wave power is at most a factor ~1–20. This residual discrepancy can be explained by faster than quasilinear diffusion mechanisms, such as nonlinear phase bunching which rapidly transports electrons into the loss cone (Albert et al., 2013; Bortnik et al., 2008; Karpman & Shklyar, 1977; D. R. Shklyar, 2021; D. R. Shklyar & Matsumoto, 2009). Large-amplitude transmitter waves in our local BLC wisp precipitation events are possible because the majority of the inferred transmitter WNAs $\theta \lesssim 45°$ are consistent with ducted propagation based on wisp dispersion fitting (Table S1 in Supporting Information S1 and Figure 6). These large-amplitude transmitter waves have been occasionally observed by the Van Allen Probes as shown in Figure 1 (>4 mV/m compared with statistical wave amplitudes of ~0.05 mV/m in Ma et al. [2022]). On the global scale, Claudepierre et al. (2020) have also reported a discrepancy between the quasilinearly calculated and observed lifetimes of inner belt ($L < 2.5$) energetic electrons by more than 1 order of magnitude. Although Coulomb energy drag has been suggested by the authors to be potentially capable of reducing this inconsistency, this drag is most effective at $L < 1.5$ and contributes to drift-averaged diffusion rates of up to 10^{-6} s^{-1} near $L \sim 1.5$ (Abel & Thorne, 1998; Albert et al., 2020), compared with the observed wisp precipitation at $L \sim 1.6$–2.0 with diffusion rates on the order of 10^{-3} s^{-1}.

By comparing wave amplitudes estimated from quasilinear diffusion rates based on ELFIN measurements with nonlinear threshold wave amplitudes predicted by theory, we find that nonlinear effects should be taken into account, at least for these local BLC wisp precipitation events. Nonlinear interactions are likely to take place near the equatorial magnetosphere where the magnetic field inhomogeneity is small and significant power of narrowband man-made VLF transmitter waves has been observed (Gu et al., 2021; Ma et al., 2017, 2022; Z. Zhang et al., 2018). Nonetheless, nonlinear interactions associated with VLF transmitter waves can be easily suppressed by many other effects, such as very short coherent wave packets and wave amplitude modulations as outlined in Section 1 (Allanson et al., 2021; An et al., 2022; Gan et al., 2022; Tao et al., 2013; X.-J. Zhang, Mourenas, et al., 2020; X.-J. Zhang et al., 2018). Therefore, the importance of electron nonlinear scattering by transmitter waves in the inner belt has yet to be tested statistically in the future.

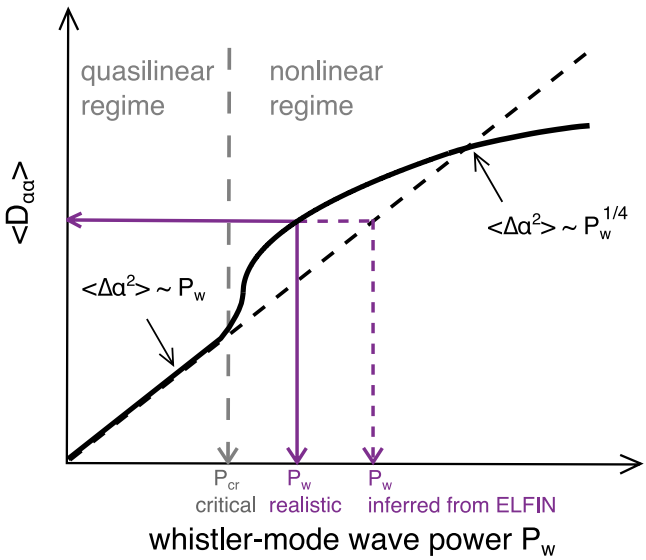

Figure 8. Diagram of electron pitch angle diffusion rates $D_{\alpha\alpha}$ as a function of whistler-mode transmitter very low frequency (VLF) wave power $P_w = B_w^2$. In the nonlinear regime, the wave amplitudes inferred from Electron Loss and Fields Investigation (ELFIN)-measured diffusion rates based on the quasilinear theory will overestimate the actual wave amplitudes.

We have demonstrated in a few BLC wisp precipitation events that nonlinear wave thresholds have been well surpassed near the equator, according to quasilinear wave amplitude estimates from ELFIN measurements. However, it is worth emphasizing that the derived transmitter wave amplitudes in our wisp precipitation events are only intended to underscore the necessity of including nonlinear wave–particle interactions for intense near-monochromatic VLF transmitter waves. In the nonlinear regime, our quasilinear calculations will overestimate the actual transmitter wave amplitudes. To illustrate this, Figure 8 presents a schematic of electron pitch angle diffusion rates as a function of VLF transmitter wave power $P_w = B_w^2$. When the wave power P_w is smaller than the critical nonlinear threshold wave power P_{cr}, the diffusion rate $D_{\alpha\alpha}$ scales linearly with the VLF transmitter wave power P_w (Kennel & Engelmann, 1966). When $P_w > P_{cr}$, nonlinear phase bunching or trapping occurs. These nonlinear effects quickly move and mix electron in the energy/pitch angle space (Artemyev, Neishtadt, Vasiliev, Zhang, et al., 2021) and provide a large effective diffusion rate $D_{\alpha\alpha}$ varying with P_w as $\sim P_w^{1/4}$ (Artemyev, Neishtadt, Vasiliev, & Mourenas, 2021). Thus, for the large $D_{\alpha\alpha}$ values inferred from ELFIN measurements in the BLC wisp precipitation events, the quasilinear diffusion model predicts a transmitter wave power according to the linear relation, which will clearly overestimate the real wave power in the nonlinear regime.

9. Conclusions

In this paper, we have statistically investigated the inner belt wisp precipitation events measured by the ELFIN energetic electron detector at $L \lesssim 2$ between March 2021 and April 2022. Of the 646 inner belt ELFIN measurements, 82 wisp events have been recorded in the energy range of 50 to ∼500 keV; 62 events showed only DLC electron fluxes and 18 events showed detectable BLC electron fluxes. These BLC wisp precipitation events provide new information on inner belt energetic electron scattering and losses induced by VLF transmitter waves, compared with previous similar studies in which only DLC wisps were reported (see, e.g., X. Li et al., 2012; Sauvaud et al., 2008). Detailed analyses of the wisp precipitation events have led to the following findings:

1. The majority of wisp precipitation events, with fluxes either in the BLC or in the DLC, tend to occur in the longitudinal range of ∼100° to ∼250° east of the SAA region, and at *MLT* of ∼1–7 hr where VLF transmitter wave power has been observed to be higher in previous studies (e.g., Ma et al., 2017). BLC wisp precipitation events are more likely to be observed in the Northern Hemisphere and within the longitudes of ∼160° to ∼220°, where the NPM transmitter station (∼202° longitude) resides nearby. Only two BLC wisp precipitation events have been detected near the most powerful transmitter of NWC and two events take place near HWU. This occurrence pattern may be explained by increased trapped/quasi-trapped fluxes with increasing longitudinal distance eastward of the SAA, by higher trapped/quasi-trapped fluxes at the edge of a wider northern BLC in this region, by a larger local wave power near the individual northern VLF stations, and by limited orbital coverage near the NWC station. The occurrence rate of BLC wisp precipitation is generally less than ∼20% in local *MLT* and longitudes where they have been mostly observed and is only ∼3% when taking into account all ELFIN measurements in the inner belt.
2. Combining magnetic field and plasmaspheric models, quasilinear theory, and ELFIN observations of full wisp pitch angle distributions with BLC fluxes, we have obtained wisp electron bounce-averaged pitch angle diffusion coefficients of the order of 10^{-4} to 10^{-2} s^{-1}. The inferred diffusion rates are several orders of magnitude larger than model diffusion rates of up to 10^{-6} s^{-1} calculated from global and statistical averages of transmitter wave power (e.g., Ma et al., 2022; Ross et al., 2019).
3. These large pitch angle diffusion coefficients have been utilized to deduce the associated local VLF transmitter wave amplitudes near the equator, based on quasilinear calculations from a transmitter-induced electron scattering model (Ma et al., 2022). The inferred transmitter wave amplitudes of ∼2–30 mV/m well exceed the threshold amplitudes for nonlinear interactions near the equator predicted by theories. Thus, it is necessary to include nonlinear effects associated with energetic electron scattering by intense transmitter waves, at least

for the local BLC wisp precipitation events observed by ELFIN. In the nonlinear regime, the wave amplitudes inferred based on quasilinear theory probably overestimate the real wave amplitudes.

Data Availability Statement

ELFIN data can be accessed through http://data.elfin.ucla.edu/. Data analysis was done using SPEDAS V4.1, see Angelopoulos et al. (2019).

Acknowledgments
Y.S., A.V.A., X.-J.Z., and V.A. acknowledge support by NASA awards 80NSSC20K1578 and 80NSSC23K0089 and NSF Grants AGS-1242918, AGS-2019950, AGS-2021749, and 2026375. Q.M. acknowledges the support by NASA Grant 80NSSC20K0196. We are grateful to NASA's CubeSat Launch Initiative for ELFIN's successful launch in the desired orbits. We acknowledge early support of ELFIN project by the AFOSR, under its University Nanosat Program, UNP-8 project, contract FA9453-12-D-0285, and by the California Space grant program. We acknowledge critical contributions of numerous volunteer ELFIN team student members.

References

Abel, B., & Thorne, R. M. (1998). Electron scattering loss in Earth's inner magnetosphere: 1. Dominant physical processes. *Journal of Geophysical Research*, *103*(A2), 2385–2396. https://doi.org/10.1029/97JA02919

Agapitov, O. V., Artemyev, A. V., Mourenas, D., Kasahara, Y., & Krasnoselskikh, V. (2014). Inner belt and slot region electron lifetimes and energization rates based on AKEBONO statistics of whistler waves. *Journal of Geophysical Research: Space Physics*, *119*, 2876–2893. https://doi.org/10.1002/2014JA019886

Albert, J. M. (2001). Comparison of pitch angle diffusion by turbulent and monochromatic whistler waves. *Journal of Geophysical Research*, *106*(A5), 8477–8482. https://doi.org/10.1029/2000JA000304

Albert, J. M. (2002). Nonlinear interaction of outer zone electrons with VLF waves. *Geophysical Research Letters*, *29*(8), 1275. https://doi.org/10.1029/2001GL013941

Albert, J. M. (2010). Diffusion by one wave and by many waves. *Journal of Geophysical Research*, *115*, A00F05. https://doi.org/10.1029/2009JA014732

Albert, J. M., Starks, M. J., Selesnick, R. S., Ling, A. G., O'Malley, S., & Quinn, R. A. (2020). VLF transmitters and lightning-generated whistlers: 2. Diffusion of radiation belt electrons. *Journal of Geophysical Research: Space Physics*, *125*, e2019JA027030. https://doi.org/10.1029/2019JA027030

Albert, J. M., Tao, X., & Bortnik, J. (2013). Aspects of nonlinear wave–particle interactions. In D. Summers, I. U. Mann, D. N. Baker, & M. Schulz (Eds.), *Dynamics of the Earth's radiation belts and inner magnetosphere* (pp. 255–264). https://doi.org/10.1029/2012GM001324

Alken, P., Thébault, E., Beggan, C. D., Amit, H., Aubert, J., Baerenzung, J., et al. (2021). International geomagnetic reference field: The thirteenth generation. *Earth Planets and Space*, *73*(1), 49. https://doi.org/10.1186/s40623-020-01288-x

Allanson, O., Watt, C. E. J., Allison, H. J., & Ratcliffe, H. (2021). Electron diffusion and advection during nonlinear interactions with whistler-mode waves. *Journal of Geophysical Research: Space Physics*, *126*, e2020JA028793. https://doi.org/10.1029/2020JA028793

An, Z., Wu, Y., & Tao, X. (2022). Electron dynamics in a chorus wave field generated from particle-in-cell simulations. *Geophysical Research Letters*, *49*, e2022GL097778. https://doi.org/10.1029/2022GL097778

Andronov, A. A., & Trakhtengerts, V. Y. (1964). Kinetic instability of the Earth's outer radiation belt. *Geomagnetism and Aeronomy*, *4*, 233–242.

Angelopoulos, V., Cruce, P., Drozdov, A., Grimes, E. W., Hatzigeorgiu, N., King, D. A., et al. (2019). The Space Physics Environment Data Analysis System (SPEDAS). *Space Science Reviews*, *215*(1), 9. https://doi.org/10.1007/s11214-018-0576-4

Angelopoulos, V., Tsai, E., Bingley, L., Shaffer, C., Turner, D. L., Runov, A., et al. (2020). The ELFIN Mission. arXiv e-prints, arXiv:2006.07747.

Artemyev, A. V., Agapitov, O., Mourenas, D., Krasnoselskikh, V., Shastun, V., & Mozer, F. (2016). Oblique whistler-mode waves in the Earth's inner magnetosphere: Energy distribution, origins, and role in radiation belt dynamics. *Space Science Reviews*, *200*(1–4), 261–355. https://doi.org/10.1007/s11214-016-0252-5

Artemyev, A. V., Mourenas, D., Agapitov, O. V., & Krasnoselskikh, V. V. (2013). Parametric validations of analytical lifetime estimates for radiation belt electron diffusion by whistler waves. *Annales Geophysicae*, *31*(4), 599–624. https://doi.org/10.5194/angeo-31-599-2013

Artemyev, A. V., Mourenas, D., Agapitov, O. V., Vainchtein, D. L., Mozer, F. S., & Krasnoselskikh, V. V. (2015). Stability of relativistic electron trapping by strong whistler or electromagnetic ion cyclotron waves. *Physics of Plasmas*, *22*(8), 082901. https://doi.org/10.1063/1.4927774

Artemyev, A. V., Neishtadt, A. I., Vainchtein, D. L., Vasiliev, A. A., Vasko, I. Y., & Zelenyi, L. M. (2018). Trapping (capture) into resonance and scattering on resonance: Summary of results for space plasma systems. *Communications in Nonlinear Science and Numerical Simulations*, *65*, 111–160. https://doi.org/10.1016/j.cnsns.2018.05.004

Artemyev, A. V., Neishtadt, A. I., Vasiliev, A. A., & Mourenas, D. (2021). Transitional regime of electron resonant interaction with whistler-mode waves in inhomogeneous space plasma. *Physical Review E: Statistical Physics, Plasmas, Fluids, and Related Interdisciplinary Topics*, *104*(5), 055203. https://doi.org/10.1103/PhysRevE.104.055203

Artemyev, A. V., Neishtadt, A. I., Vasiliev, A. A., Zhang, X.-J., Mourenas, D., & Vainchtein, D. (2021). Long-term dynamics driven by resonant wave–particle interactions: From Hamiltonian resonance theory to phase space mapping. *Journal of Plasma Physics*, *87*(2), 835870201. https://doi.org/10.1017/S0022377821000246

Bell, T. F. (1986). The wave magnetic field amplitude threshold for nonlinear trapping of energetic gyroresonant and Landau resonant electrons by nonducted VLF waves in the magnetosphere. *Journal of Geophysical Research*, *91*(A4), 4365–4379. https://doi.org/10.1029/JA091iA04p04365

Bortnik, J., Thorne, R. M., & Inan, U. S. (2008). Nonlinear interaction of energetic electrons with large amplitude chorus. *Geophysical Research Letters*, *35*, L21102. https://doi.org/10.1029/2008GL035500

Brinca, A. L. (1980). On the evolution of the geomagnetospheric coherent cyclotron resonance in the midst of noise. *Journal of Geophysical Research*, *85*(A9), 4711–4714. https://doi.org/10.1029/JA085iA09p04711

Claudepierre, S. G., Ma, Q., Bortnik, J., O'Brien, T. P., Fennell, J. F., & Blake, J. B. (2020). Empirically estimated electron lifetimes in the Earth's radiation belts: Comparison with theory. *Geophysical Research Letters*, *47*, e2019GL086056. https://doi.org/10.1029/2019GL086056

Clilverd, M. A., & Horne, R. B. (1996). Ground-based evidence of latitude-dependent cyclotron absorption of whistler mode signals originating from VLF transmitters. *Journal of Geophysical Research*, *101*(A2), 2355–2368. https://doi.org/10.1029/95JA03153

Clilverd, M. A., Rodger, C. J., Gamble, R. G., Meredith, N. P., Parrot, M., Berthelier, J.-J., & Thomson, N. R. (2008). Ground-based transmitter signals observed from space: Ducted or nonducted? *Journal of Geophysical Research*, *113*, A04211. https://doi.org/10.1029/2007JA012602

Cohen, M. B., Inan, U. S., & Paschal, E. W. (2010). Sensitive broadband ELF/VLF radio reception with the AWESOME instrument. *IEEE Transactions on Geoscience and Remote Sensing*, *48*(1), 3–17. https://doi.org/10.1109/TGRS.2009.2028334

Datlowe, D. W., & Imhof, W. L. (1990). Cyclotron resonance precipitation of energetic electrons from the inner magnetosphere. *Journal of Geophysical Research*, *95*(A5), 6477–6491. https://doi.org/10.1029/JA095iA05p06477

Dowden, R. L. (1982). Detrapping by an additional wave of wave-trapped electrons. *Journal of Geophysical Research*, *87*(A8), 6237–6242. https://doi.org/10.1029/JA087iA08p06237

Drummond, W. E., & Pines, D. (1962). Non-linear stability of plasma oscillations. *Nuclear Fusion Supplement*, *3*, 1049–1058.

Gamble, R. J., Rodger, C. J., Clilverd, M. A., Sauvaud, J.-A., Thomson, N. R., Stewart, S. L., et al. (2008). Radiation belt electron precipitation by man-made VLF transmissions. *Journal of Geophysical Research*, *113*, A10211. https://doi.org/10.1029/2008JA013369

Gan, L., Li, W., Ma, Q., Albert, J. M., Artemyev, A. V., & Bortnik, J. (2020). Nonlinear interactions between radiation belt electrons and chorus waves: Dependence on wave amplitude modulation. *Geophysical Research Letters*, *47*, e2019GL085987. https://doi.org/10.1029/2019GL085987

Gan, L., Li, W., Ma, Q., Artemyev, A. V., & Albert, J. M. (2022). Dependence of nonlinear effects on whistler-mode wave bandwidth and amplitude: A perspective from diffusion coefficients. *Journal of Geophysical Research: Space Physics*, *127*, e2021JA030063. https://doi.org/10.1029/2021JA030063

Gu, W., Chen, L., Xia, Z., & Horne, R. B. (2021). Direct evidence reveals transmitter signal propagation in the magnetosphere. *Geophysical Research Letters*, *48*, e2021GL093987. https://doi.org/10.1029/2021GL093987

Helliwell, R. A. (1965). *Whistlers and related ionospheric phenomena*. Stanford University Press.

Helliwell, R. A., & Katsufrakis, J. P. (1974). VLF wave injection into the magnetosphere from Siple Station, Antarctica. *Journal of Geophysical Research*, *79*(16), 2511–2518. https://doi.org/10.1029/JA079i016p02511

Hua, M., Li, W., Ni, B., Ma, Q., Green, A., Shen, X., et al. (2020). Very-low-frequency transmitters bifurcate energetic electron belt in near-Earth space. *Nature Communications*, *11*(1), 4847. https://doi.org/10.1038/s41467-020-18545-y

Imhof, W. L., Reagan, J. B., Voss, H. D., Gaines, E. E., Datlowe, D. W., Mobilia, J., et al. (1983). Direct observation of radiation belt electrons precipitated by the controlled injection of VLF signals from a ground-based transmitter. *Geophysical Research Letters*, *10*(4), 361–364. https://doi.org/10.1029/GL010i004p00361

Inan, U. S., Bell, T. F., & Helliwell, R. A. (1978). Nonlinear pitch angle scattering of energetic electrons by coherent VLF waves in the magnetosphere. *Journal of Geophysical Research*, *83*(A7), 3235–3254. https://doi.org/10.1029/JA083iA07p03235

Inan, U. S., Golkowski, M., Casey, M. K., Moore, R. C., Peter, W., Kulkarni, P., et al. (2007). Subionospheric VLF observations of transmitter-induced precipitation of inner radiation belt electrons. *Geophysical Research Letters*, *34*, L02106. https://doi.org/10.1029/2006GL028494

Karpman, V. I. (1974). Nonlinear effects in the ELF waves propagating along the magnetic field in the magnetosphere. *Space Science Reviews*, *16*(3), 361–388. https://doi.org/10.1007/BF00171564

Karpman, V. I., Istomin, J. N., & Shklyar, D. R. (1974). Nonlinear theory of a quasi-monochromatic whistler mode packet in inhomogeneous plasma. *Plasma Physics*, *16*(8), 685–703. https://doi.org/10.1088/0032-1028/16/8/001

Karpman, V. I., & Shklyar, D. R. (1977). Particle precipitation caused by a single whistler-mode wave injected into the magnetosphere. *Planetary and Space Science*, *25*(4), 395–403. https://doi.org/10.1016/0032-0633(77)90055-1

Kennel, C. F., & Engelmann, F. (1966). Velocity space diffusion from weak plasma turbulence in a magnetic field. *Physics of Fluids*, *9*(12), 2377–2388. https://doi.org/10.1063/1.1761629

Kennel, C. F., & Petschek, H. E. (1966). Limit on stably trapped particle fluxes. *Journal of Geophysical Research*, *71*(1), 1–28. https://doi.org/10.1029/JZ071i001p00001

Koons, H. C., Edgar, B. C., & Vampola, A. L. (1981). Precipitation of inner zone electrons by whistler mode waves from the VLF transmitters UMS and NWC. *Journal of Geophysical Research*, *86*(A2), 640–648. https://doi.org/10.1029/JA086iA02p00640

Kulkarni, P., Inan, U. S., Bell, T. F., & Bortnik, J. (2008). Precipitation signatures of ground-based VLF transmitters. *Journal of Geophysical Research*, *113*, A07214. https://doi.org/10.1029/2007JA012569

Lehtinen, N. G., & Inan, U. S. (2009). Full-wave modeling of transionospheric propagation of VLF waves. *Geophysical Research Letters*, *36*, L03104. https://doi.org/10.1029/2008GL036535

Li, W., Bortnik, J., Thorne, R. M., Cully, C. M., Chen, L., Angelopoulos, V., et al. (2013). Characteristics of the Poynting flux and wave normal vectors of whistler-mode waves observed on THEMIS. *Journal of Geophysical Research*, *118*, 1461–1471. https://doi.org/10.1002/jgra.50176

Li, W., Ni, B., Thorne, R. M., Bortnik, J., Green, J. C., Kletzing, C. A., et al. (2013). Constructing the global distribution of chorus wave intensity using measurements of electrons by the POES satellites and waves by the Van Allen Probes. *Geophysical Research Letters*, *40*, 4526–4532. https://doi.org/10.1002/grl.50920

Li, X., Ma, Y., Wang, P., Wang, H., Lu, H., Zhang, X., et al. (2012). Study of the North West Cape electron belts observed by DEMETER satellite. *Journal of Geophysical Research*, *117*, A04201. https://doi.org/10.1029/2011JA017121

Liu, Y., Xiang, Z., Ni, B., Li, X., Zhang, K., Fu, S., et al. (2022). Quasi-trapped electron fluxes induced by NWC transmitter and CRAND: Observations and simulations. *Geophysical Research Letters*, *49*, e2021GL097443. https://doi.org/10.1029/2021GL097443

Ma, Q., Gu, W., Claudepierre, S. G., Li, W., Bortnik, J., Hua, M., & Shen, X. C. (2022). Electron scattering by very-low-frequency and low-frequency waves from ground transmitters in the Earth's inner radiation belt and slot region. *Journal of Geophysical Research: Space Physics*, *127*, e2022JA030349. https://doi.org/10.1029/2022JA030349

Ma, Q., Mourenas, D., Li, W., Artemyev, A., & Thorne, R. M. (2017). VLF waves from ground-based transmitters observed by the Van Allen Probes: Statistical model and effects on plasmaspheric electrons. *Geophysical Research Letters*, *44*, 6483–6491. https://doi.org/10.1002/2017GL073885

Meredith, N. P., Horne, R. B., Clilverd, M. A., & Ross, J. P. J. (2019). An investigation of VLF transmitter wave power in the inner radiation belt and slot region. *Journal of Geophysical Research: Space Physics*, *124*, 5246–5259. https://doi.org/10.1029/2019JA026715

Mourenas, D., Artemyev, A. V., Zhang, X. J., Angelopoulos, V., Tsai, E., & Wilkins, C. (2021). Electron lifetimes and diffusion rates inferred from ELFIN measurements at low altitude: First results. *Journal of Geophysical Research: Space Physics*, *126*, e2021JA029757. https://doi.org/10.1029/2021JA029757

Mourenas, D., Zhang, X.-J., Artemyev, A. V., Angelopoulos, V., Thorne, R. M., Bortnik, J., et al. (2018). Electron nonlinear resonant interaction with short and intense parallel chorus wave packets. *Journal of Geophysical Research*, *123*, 4979–4999. https://doi.org/10.1029/2018JA025417

Ni, B., Li, W., Thorne, R. M., Bortnik, J., Green, J. C., Kletzing, C. A., et al. (2014). A novel technique to construct the global distribution of whistler mode chorus wave intensity using low-altitude POES electron data. *Journal of Geophysical Research: Space Physics*, *119*, 5685–5699. https://doi.org/10.1002/2014JA019935

Ni, B., Thorne, R. M., Meredith, N. P., Shprits, Y. Y., & Horne, R. B. (2011). Diffuse auroral scattering by whistler mode chorus waves: Dependence on wave normal angle distribution. *Journal of Geophysical Research*, *116*, A10207. https://doi.org/10.1029/2011JA016517

Nunn, D. (1974). A self-consistent theory of triggered VLF emissions. *Planetary and Space Science*, *22*(3), 349–378. https://doi.org/10.1016/0032-0633(74)90070-1

Nunn, D. (1986). A nonlinear theory of sideband stability in ducted whistler mode waves. *Planetary and Space Science*, *34*(5), 429–451. https://doi.org/10.1016/0032-0633(86)90032-2

Omura, Y., Katoh, Y., & Summers, D. (2008). Theory and simulation of the generation of whistler-mode chorus. *Journal of Geophysical Research*, *113*, A04223. https://doi.org/10.1029/2007JA012622

Omura, Y., Matsumoto, H., Nunn, D., & Rycroft, M. J. (1991). A review of observational, theoretical and numerical studies of VLF triggered emissions. *Journal of Atmospheric and Terrestrial Physics*, *53*(5), 351–368. https://doi.org/10.1016/0021-9169(91)90031-2

Omura, Y., Nunn, D., & Summers, D. (2013). Generation processes of whistler mode chorus emissions: Current status of nonlinear wave growth theory. In D. Summers, I. U. Mann, D. N. Baker, & M. Schulz (Eds.), *Dynamics of the Earth's radiation belts and inner magnetosphere* (pp. 243–254). https://doi.org/10.1029/2012GM001347

Ozhogin, P., Tu, J., Song, P., & Reinisch, B. W. (2012). Field-aligned distribution of the plasmaspheric electron density: An empirical model derived from the IMAGE RPI measurements. *Journal of Geophysical Research*, *117*, A06225. https://doi.org/10.1029/2011JA017330

Reidy, J. A., Horne, R. B., Glauert, S. A., Clilverd, M. A., Meredith, N. P., Woodfield, E. E., et al. (2021). Comparing electron precipitation fluxes calculated from pitch angle diffusion coefficients to LEO satellite observations. *Journal of Geophysical Research: Space Physics*, *126*, e2020JA028410. https://doi.org/10.1029/2020JA028410

Ross, J. P. J., Meredith, N. P., Glauert, S. A., Horne, R. B., & Clilverd, M. A. (2019). Effects of VLF transmitter waves on the inner belt and slot region. *Journal of Geophysical Research: Space Physics*, *124*, 5260–5277. https://doi.org/10.1029/2019JA026716

Sauvaud, J. A., Maggiolo, R., Jacquey, C., Parrot, M., Berthelier, J. J., Gamble, R. J., & Rodger, C. J. (2008). Radiation belt electron precipitation due to VLF transmitters: Satellite observations. *Geophysical Research Letters*, *35*, L09101. https://doi.org/10.1029/2008GL033194

Sauvaud, J. A., Moreau, T., Maggiolo, R., Treilhou, J.-P., Jacquey, C., Cros, A., et al. (2006). High-energy electron detection onboard DEMETER: The IDP spectrometer, description and first results on the inner belt. *Planetary and Space Science*, *54*(5), 502–511. https://doi.org/10.1016/j.pss.2005.10.019

Selesnick, R. S., Albert, J. M., & Starks, M. J. (2013). Influence of a ground-based VLF radio transmitter on the inner electron radiation belt. *Journal of Geophysical Research: Space Physics*, *118*, 628–635. https://doi.org/10.1002/jgra.50095

Shapiro, V. D., & Sagdeev, R. Z. (1997). Nonlinear wave–particle interaction and conditions for the applicability of quasilinear theory. *Physics Reports*, *283*(1–4), 49–71. https://doi.org/10.1016/S0370-1573(96)00053-1

Shklyar, D., & Luzhkovskiy, A. (2022). Self-consistent amplitude profile of ducted VLF transmitter signal due to resonant interaction with energetic electrons in the magnetosphere. *Advances in Space Research*. https://doi.org/10.1016/j.asr.2022.08.081

Shklyar, D. R. (2021). A theory of interaction between relativistic electrons and magnetospherically reflected whistlers. *Journal of Geophysical Research: Space Physics*, *126*, e2020JA028799. https://doi.org/10.1029/2020JA028799

Shklyar, D. R., & Jiříček, F. (2000). Simulation of nonducted whistler spectrograms observed aboard the MAGION 4 and 5 satellites. *Journal of Atmospheric and Solar-Terrestrial Physics*, *62*, 347–370. https://doi.org/10.1016/S1364-6826(99)00097-8

Shklyar, D. R., & Matsumoto, H. (2009). Oblique whistler-mode waves in the inhomogeneous magnetospheric plasma: Resonant interactions with energetic charged particles. *Surveys in Geophysics*, *30*(2), 55–104. https://doi.org/10.1007/s10712-009-9061-7

Smith, R. L., Helliwell, R. A., & Yabroff, I. W. (1960). A theory of trapping of whistlers in field-aligned columns of enhanced ionization. *Journal of Geophysical Research*, *65*(3), 815–823. https://doi.org/10.1029/JZ065i003p00815

Starks, M. J., Albert, J. M., Ling, A. G., O'Malley, S., & Quinn, R. A. (2020). VLF transmitters and lightning-generated whistlers: 1. Modeling waves from source to space. *Journal of Geophysical Research: Space Physics*, *125*, e2019JA027029. https://doi.org/10.1029/2019JA027029

Starks, M. J., Quinn, R. A., Ginet, G. P., Albert, J. M., Sales, G. S., Reinisch, B. W., & Song, P. (2008). Illumination of the plasmasphere by terrestrial very low frequency transmitters: Model validation. *Journal of Geophysical Research*, *113*, A09320. https://doi.org/10.1029/2008JA013112

Tao, X., Bortnik, J., Albert, J. M., & Thorne, R. M. (2012). Comparison of bounce-averaged quasi-linear diffusion coefficients for parallel propagating whistler mode waves with test particle simulations. *Journal of Geophysical Research*, *117*, A10205. https://doi.org/10.1029/2012JA017931

Tao, X., Bortnik, J., Albert, J. M., Thorne, R. M., & Li, W. (2013). The importance of amplitude modulation in nonlinear interactions between electrons and large amplitude whistler waves. *Journal of Atmospheric and Solar-Terrestrial Physics*, *99*, 67–72. https://doi.org/10.1016/j.jastp.2012.05.012

Thorne, R. M. (2010). Radiation belt dynamics: The importance of wave–particle interactions. *Geophysical Research Letters*, *372*, L22107. https://doi.org/10.1029/2010GL044990

Thorne, R. M., & Horne, R. B. (1994). Landau damping of magnetospherically reflected whistlers. *Journal of Geophysical Research*, *99*(A9), 17249–17258. https://doi.org/10.1029/94JA01006

Tu, W., Selesnick, R., Li, X., & Looper, M. (2010). Quantification of the precipitation loss of radiation belt electrons observed by SAMPEX. *Journal of Geophysical Research*, *115*, A07210. https://doi.org/10.1029/2009JA014949

Vampola, A. L., & Kuck, G. A. (1978). Induced precipitation of inner zone electrons: 1. Observations. *Journal of Geophysical Research*, *83*(A6), 2543–2551. https://doi.org/10.1029/JA083iA06p02543

Vedenov, A. A., Velikhov, E., & Sagdeev, R. (1962). Quasilinear theory of plasma oscillations. *Nuclear Fusion Supplement*, *2*, 465–475.

Zhang, X.-J., Agapitov, O., Artemyev, A. V., Mourenas, D., Angelopoulos, V., Kurth, W. S., et al. (2020). Phase decoherence within intense chorus wave packets constrains the efficiency of nonlinear resonant electron acceleration. *Geophysical Research Letters*, *47*, e2020GL089807. https://doi.org/10.1029/2020GL089807

Zhang, X.-J., Mourenas, D., Artemyev, A. V., Angelopoulos, V., Kurth, W. S., Kletzing, C. A., & Hospodarsky, G. B. (2020). Rapid frequency variations within intense chorus wave packets. *Geophysical Research Letters*, *47*, e2020GL088853. https://doi.org/10.1029/2020GL088853

Zhang, X.-J., Thorne, R., Artemyev, A., Mourenas, D., Angelopoulos, V., Bortnik, J., et al. (2018). Properties of intense field-aligned lower-band chorus waves: Implications for nonlinear wave–particle interactions. *Journal of Geophysical Research: Space Physics*, *123*, 5379–5393. https://doi.org/10.1029/2018JA025390

Zhang, Z., Chen, L., Li, X., Xia, Z., Heelis, R. A., & Horne, R. B. (2018). Observed propagation route of VLF transmitter signals in the magnetosphere. *Journal of Geophysical Research: Space Physics*, *123*, 5528–5537. https://doi.org/10.1029/2018JA025637